Introduction

Cancers of the nasal cavity and paranasal sinuses (NCPS) are rare and account for only 5% of all head-and-neck cancers (1). Limited anatomic access makes early diagnosis difficult, and the presence of air-filled spaces permits asymptomatic growth until the invasion of an adjacent structure produces symptoms. Hence, most patients come to the hospital with an advanced stage. Complete surgical resection followed by postoperative radiotherapy is associated with the best outcome in patients diagnosed with cancer of the NCPS (2–4). Unfortunately, some patients are diagnosed with unresectable disease involving adjacent structures such as the nasopharynx, clivus, middle cranial fossa, brain, or orbita. These patients are not candidates for gross total resection and are typically treated with either definitive radiotherapy or a combination of chemotherapy and radiotherapy.

Most studies of NCPS cancer are small and include a variety of histologic findings, treatment modalities, and disease stage (2, 5–7). Hence, these studies are limited in their analysis and discussion regarding the effects of radiotherapy on patients with unresectable disease. To our knowledge the outcomes of patients with unresectable cancers of the NCPS of limited histology types treated with radiotherapy have been rarely reported in past medical literature (8).

A proton beam enables a rapidly increasing dose at the end of the beam range (9). Because of its excellent dose escalation characteristics, proton beam therapy (PBT) is expected for the treatment of NCPS cancer, enabling the delivery of a high radiation dose to the tumor but not exceeding the tolerant radiation dose to close critical organs, such as the optical nerve, brainstem, and brain. However, because of the small number of patients and facilities, only a few reports of the clinical outcome of NCPS cancer treated using PBT have been made, most of which included patients with a variety of histologic types, disease stages, and concurrent treatment modalities (10–13).

The present study describes our experience treating patients with unresectable Stage IV and local recurrent carcinoma of the NCPS using PBT.

Methods and Materials

Patients

Between 2001 and 2007, a total of 102 head-and-neck cancer patients were treated at the Proton Medical Research Center, University of Tsukuba, Japan. Among them, 17 patients (13 men, 4 women; median age, 62 years; range, 30–83 years) who were diagnosed as having unresectable carcinoma of the NCPS (identified by International Classification of Disease, 10th Revision codes) were evaluated.

The histology was squamous cell carcinoma in 11 patients, adenocarcinoma in 2 patients, adenoid cystic carcinoma in 2 patients, and myoepithelial cell carcinoma in 1 patient. Patients with melanoma, sarcoma, lymphoma, rhabdomyosarcoma, or esthesioneuroblastoma and pediatric patients were excluded. The pretreatment evaluation included a complete history, biopsy-proven histologic findings, physical examination, direct flexible fiberoptic endoscopic examination, blood sampling tests, and computed tomography, magnetic resonance imaging, and ultrasound examinations. The primary tumor site was nasal cavity in 3 patients, frontal sinus in 1 patient, ethmoid sinus in 9 patients, and maxillary sinus in 4 patients. One patient with frontal sinus tumor was staged in the same way as for the ethmoid sinus tumor. Lymph node metastasis was identified in 1 patient in ipsilateral retropharyngeal and bilateral Level II lymph nodes. The patients were retrospectively restaged using the International Union Against Cancer TNM staging system (7th edition, 2009); 5 patients had Stage IVA, 10 patients had Stage IVB, and 2 patients had recurrences. Five patients had received prior treatment (surgery in 2 patients, surgery with chemotherapy in 2 patients, and chemoradiotherapy [12 Gy] in 1 patient). Thirteen of 17 patients had tumor located close to the optic chiasm. The tumors were deemed unresectable for medical reasons in 16 patients (extension of the tumor to adjacent structure in 13 patients, postoperative recurrence in 2 patients, and age and complications in 1 patient) and because of refusal at a previous hospital 4 months earlier in 1 patient (Table 1).

Table 1 Patient characteristics

Case no.	Age (y)/sex	Site	Stage	Histology	Prior treatment
1	58/M	Ethmoid	IVA	Squamous	
2	71/M	Frontal	IVB	Squamous	
3	60/M	Nasal	rec	Adenocarcinoma	Surgery + chemotherapy
4	70/M	Ethmoid	IVB	Squamous	Surgery + chemotherapy
5	46/M	Ethmoid	IVB	Squamous	
6	47/F	Ethmoid	rec	Myoepithelial	Surgery
7	39/F	Ethmoid	IVB	Adenoid cystic	
8	81/M	Nasal	IVA	Squamous	
9	30/M	Ethmoid	IVB	Undifferentiated	Chemotherapy + radiation (12 Gy)
10	53/F	Ethmoid	IVB	Squamous	
11	67/M	Maxillary	IVA	Squamous	
12	57/F	Maxillary	IVA	Papilloma + squamous	Surgery
13	77/M	Ethmoid	IVB	Squamous	
14	62/M	Nasal	IVB	Adenoid cystic	
15	68/M	Maxillary	IVB	Squamous	
16	83/F	Maxillary	IVA	Adenocarcinoma	
17	63/M	Ethmoid	IVB	Squamous	

Abbreviations: M = male; F = female.

Table 2 Treatment characteristics

Case no.	Proton dose (GyE)	Proton dose/fx (GyE)	X-ray dose (Gy)	X-ray dose/fx (Gy)	Total dose (GyE)	Concurrent treatment
1	22.0	2.2	50.4	1.8	72.4	Antrotomy
2	33.0	1.7	45.0	1.8	78.0*	
3	82.5	2.1			82.5	
4	81.7	2.2			81.7	
5	79.2	2.2			79.2	
6	79.2	2.2			79.2	
7	79.2	2.2			79.2	
8	79.2	2.2			79.2	
9	66.0	2.2			78.0	
10	79.2	2.2			79.2	
11	77.2	2.0			77.2	Antrotomy + chemotherapy (S-1)
12	28.6	2.2	61.0	1.8	89.6	Chemotherapy (S-1)
13	77.0	2.2			77.0	
14	77.0	2.2			77.0	
15	77.0	2.2			77.0	
16	70.0	2.0			70.0	Antrotomy
17	74.0	2.0			74.0	

Abbreviation: fx = fraction.
* Twice-daily irradiation.

Treatment

Proton beams of 155–250 MeV were generated using a synchrotron accelerator at the Proton Medical Research Center, University of Tsukuba. All patients received PBT using the involved-field technique, and the beam delivery system created a 100% dose level homogeneously using the spread-out Bragg peak of the proton beams. The proton irradiation dose was 22–82.5 gray equivalents (GyE) over 10–39 fractions. Three patients received X-ray radiotherapy with large portals encompassing the primary tumor and neck at doses of 45, 50.4, and 61 Gy, respectively. Clinical target volume (CTV) was 38.0–338.6 cm^3 (median, 127.9 cm^3) in PBT-only patients and 17.9–120.0 cm^3 (median, 45.5 cm^3) in the 3 patients receiving boost treatment. Radiotherapy was performed 5 days per week to a total irradiation dose of 72.4–89.6 GyE over 30–64 fractions (median, 78 GyE over 36 fractions). Treatment was performed using once-daily fractionation (2.0–2.2 GyE; median, 2.2 GyE) in 16 patients and twice-daily fractionation in 1 patient (X-ray [1.8 Gy] plus proton [1.65 GyE] daily). Treatment planning was modified at most three times (median, twice) as nasal secretion or tumor response during the treatment course. Proton beam therapy was performed using coplanar treatment in all the patients. Care was taken to ensure that the irradiation dose to the brain stem and optic chiasm did not exceed 50 GyE. We used a relative biological effectiveness value of 1.0 until 2007, after which time the value was changed to 1.1. For this reason, all the irradiation doses were recalculated using a relative biological effectiveness value of 1.1 in the present study.

Concurrent treatment was performed in 4 patients (exploratory antrotomy in 2 patients, chemotherapy [S-1, a novel oral fluoropyrimidine derivative (14)] in 1 patient, and both exploratory antrotomy and chemotherapy [S-1] in 1 patient). Adjuvant chemotherapy (cisplatin plus 5-fluorouracil) was performed in 1 patient (Table 2).

Follow-up

Analysis of the treatment outcomes was based on follow-up data available as of January 2011. Patients were evaluated once per week during radiotherapy. Subsequently they were seen 1 to 2 months after irradiation, every 3 months for the next 2 to 3 years, and then every 6 months and yearly. Patients who could not come to the hospital were followed up at their primary hospital, and follow-up information was obtained from reports provided by the patients and their primary physicians. Acute and late normal tissue effects were graded according to the Radiation Therapy Oncology Group's radiation morbidity scoring criteria (15).

Statistical methods

The overall survival rate (OS) and local control rate (LC) were calculated using the Kaplan-Meier method. Because tumor growth from original site and margin was difficult to distinguish, local control was defined as no evidence of tumor growth from original site or margin. Duration was calculated from the start of radiotherapy. Prognostic factors for OS and LC that were investigated using the Wilcoxon test included extent of disease at presentation, prior treatment, tumor volume, neck lymph node involvement, histologic grade, radiation dose, and concurrent treatment. A dose–volume histogram analysis was performed for the ipsilateral and contralateral optic nerves, optic chiasm, brainstem, and ipsilateral brain surface. For the analysis the volume of the contoured optic chiasm was defined as 1.6 cm^3 on the basis of consensus of three radiation oncologists, the area of the brainstem was defined as the area between the highest level of the CTV and the cranial base, and the ipsilateral brain surface was defined as the brain surface area located behind and at the same level of the CTV with the same approximate width of gray matter.

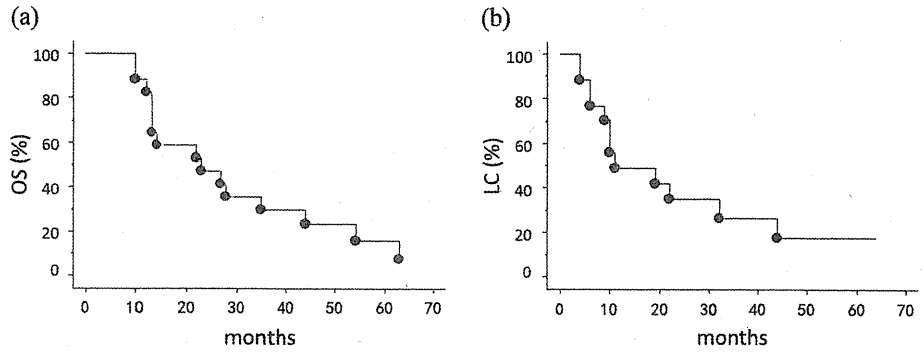

Fig. 1. (a) Overall survival rate (OS) after proton beam therapy. (b) Local control rate (LC) after proton beam therapy.

Results

Treatment outcomes

Two patients were alive and 15 patients had died as of January 2011. The median follow-up period for the surviving patients was 57 months, whereas the median follow-up period for all patients was 23 months. The OS was 47.1% at 2 years and 15.7% at 5 years (Fig. 1a).

Local recurrence developed in 12 patients and was the first site of relapse in 9 of the patients. The period until local recurrence was 10 months (range, 4–44 months). Of the 12 patients with local recurrence, 11 patients subsequently died of their disease, with a median period of 9 months (range, 2–31 months) after recurrence until death; 1 patient committed suicide. Treatment for the local recurrent tumor was symptomatic in 7 patients, chemotherapy in 3 patients, chemoradiotherapy in 1 patient, and surgery in 1 patient. The LC was 35.0% at 2 years and 17.5% at 5 years (Fig. 1b).

Metastatic lesions developed in 6 patients and were the first site of relapse in 4 patients; in the remaining 2 patients the metastatic lesions occurred simultaneously with a local recurrence. The sites of distant metastases included the neck lymph node in 3 patients, the liver in 1 patient, the lung in 1 patient, and bone in 1 patient. Among the 6 patients, 1 patient who underwent surgery for a lung metastasis has survived for 26 months, whereas the remaining 5 patients died after a median period of 11 months (range, 1–33 months) after the diagnosis of metastasis.

Overall, 2 patients showed neither a local recurrence nor metastasis for 22 and 50 months, whereas 15 patients showed a local recurrence and/or metastasis after 2–44 months (median, 9 months). In the 2 patients who died in a manner unrelated to their disease, 1 died of cardiovascular disease without evidence of carcinoma recurrence, and another died of suicide during treatment for a local recurrence.

Figures 2 and 3 each show a patient who survived for a long period after PBT.

Prognostic factors

Invasion of the frontal or sphenoid sinus and intracranial invasion was associated with OS ($p = 0.008$ and 0.012, respectively). Invasion of other area, prior treatment, tumor volume, neck lymph node involvement, histologic grade, radiation dose, and concurrent treatment were not significantly associated with OS or LC (Table 3). Figure 4 shows a case in which the irradiation dose to the optic chiasm and brainstem was controlled as tolerable.

Toxicity

Acute and late treatment-related toxicities are listed in Table 4. Grade 3 acute mucositis and dermatitis occurred in 1 patient each. In both cases the acute severe mucositis and dermatitis resolved, and no severe late mucous membrane or skin toxicity occurred. Regarding late toxicity, psychiatric symptoms accompanying brain necrosis in 1 patient (Grade 3), a bone fracture in 1 patient (Grade 4), and unilateral blindness in 1 patient (Grade 4) occurred.

The dose–volume histogram analysis is presented in Table 4. The irradiation dose to the optic chiasm had D_{max} of 73.6–0.3 GyE, whereas the D_{max} to the brainstem and brain surface were 74.5–0 GyE and 83.8–60.8 GyE, respectively.

Discussion

Unfortunately, the outcome of advanced-stage carcinoma of the NCPS is not good. Some reports have indicated an excellent survival period after treatment with intensity-modulated radiotherapy or proton beam irradiation in patients with NCPS cancer; however, these studies included many postoperative patients or early-stage patients (4, 6, 11, 12, 16–18). In a study limited to patients with locally advanced cancer of limited histology type (most were Stage III or IV), the OS was 27% at 5 years (2); in another study of patients with unresectable Stage IVB cancer, the OS was 15% (8). The results of the present study were quite similar to the results of these studies with similar patient populations. The LC (35.0% at 2 years) may be seemed as poor in PBT. However, 13 of 17 patients had tumor located close to the optic chiasm, and proton beams with extremely tight margin had to be delivered at the last stage of treatment. Of those 13 patients, 9 showed local recurrence. In contrast, 3 of 4 patients for whom a tight margin was not necessary did not show local recurrence. We consider that the unfavorable LC was caused by the many advanced-stage patients included in the present study.

Many previous reports have discussed prognostic factors for cancer of the NCPS. Tumor extent, tumor volume, radiation dose, lymph node involvement, histologic grade, and surgery are major prognostic factors among patients receiving radiation treatment

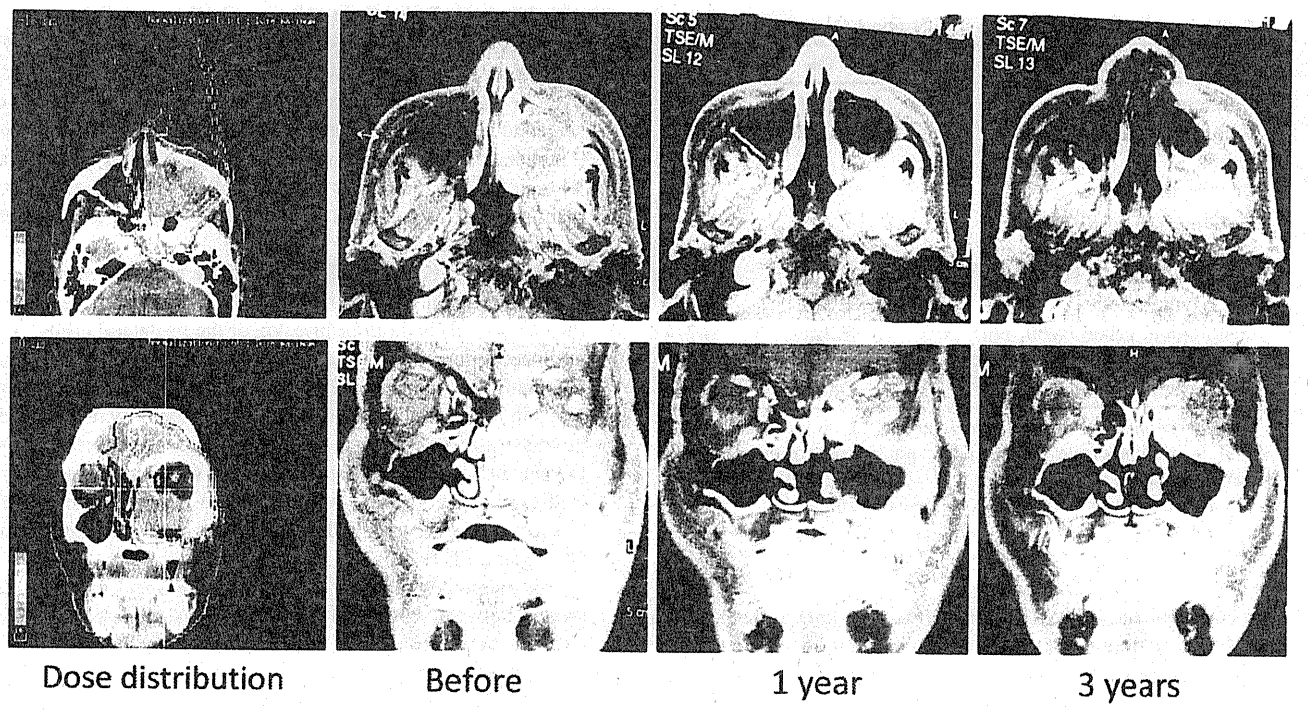

Fig. 2. A 67-year-old man with a left maxillary sinus carcinoma (T4aN0M0, Stage IVA, squamous cell carcinoma). The tumor had extended into the left orbita. An exploratory antrotomy followed by proton beam therapy (PBT) (77.22 GyE over 39 fractions) was performed in 2005. This patient was still alive as of January 2011 and had not experienced any local recurrence (64 months after PBT). Lung metastasis was operated in December 2008 (38 months after PBT). Axial (upper) and coronal (lower) images (left to right) of the dose distribution for the first plan, before treatment, 1 year, and 3 years after treatment.

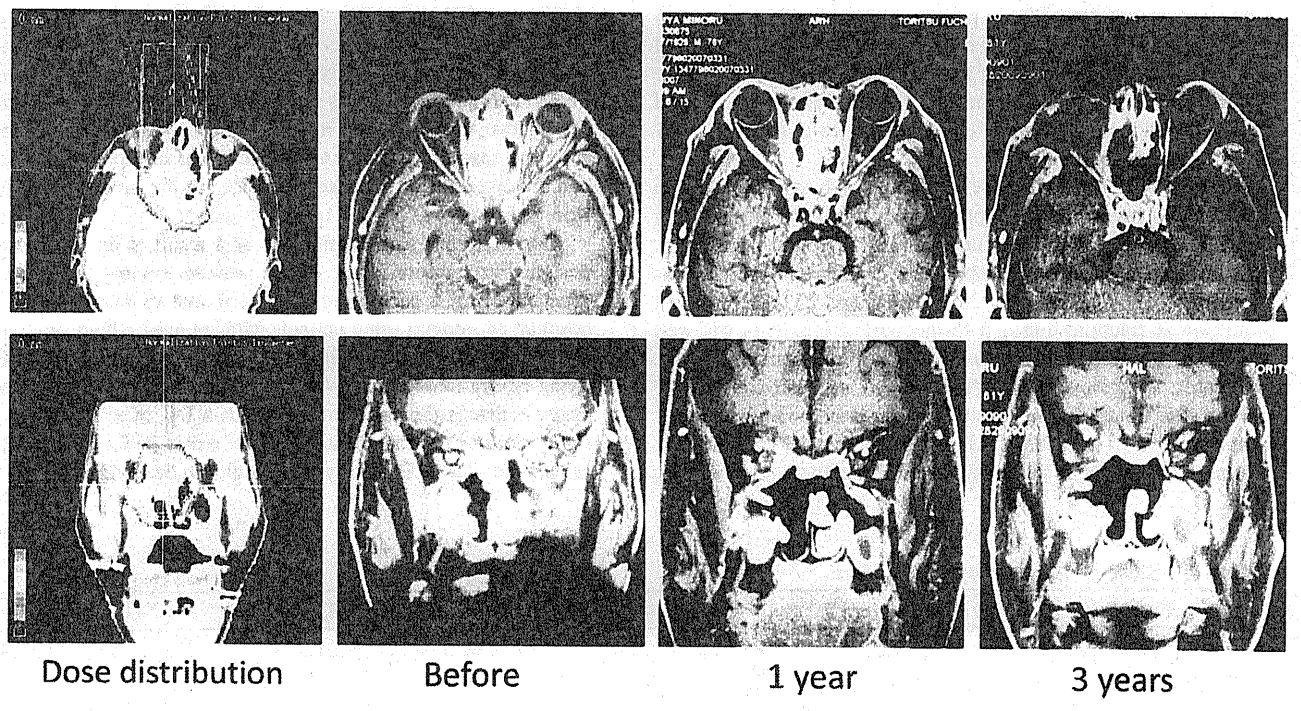

Fig. 3. A 77-year-old man with a left ethmoid sinus carcinoma (T4bN0M0, Stage IVB, squamous cell carcinoma). The tumor had extended into the right orbita, and intracranial invasion was present. Obvious tumor growth was noted between the time of treatment planning and the pretreatment study. Proton beam therapy (PBT) (77 GyE over 35 fractions) was performed in 2006. This patient was still alive as of January 2011 and had not experienced any local recurrence or metastasis (50 months after PBT). See Fig. 2 legend for an explanation of the images.

Table 3 Prognostic factors in OS and LC

Factor	OS	LC
Infratemporal fossa	0.637	0.779
Frontal or sphenoid sinus	0.008*	0.070
Orbita	0.729	0.584
Intracranium	0.012*	0.442
Nasopharynx or clivus	0.356	0.144
Prior treatment	0.214	0.191
Tumor volume ($\leq$100, >100 cm^3)	0.916	0.729
Neck lymph node	0.362	0.392
Histological grade (w/m, p/u)	0.221	0.716
Total dose ($\leq$77, >77 GyE)		0.865
Concurrent chemotherapy	0.950	0.464

Abbreviations: OS = overall survival rate; LC = local control rate; w/m = well/moderate differentiated; p/u = poorly differentiated/undifferentiated.

* Significant ($p < 0.05$) (blank = no calculation).

for cancer of the NCPS (2, 8, 12). It is well known that superior and posterior tumor extension affects patient prognosis, and tumor extent was also a prognostic factor in the present study. The OS was significantly improved in patients without invasion of the frontal or sphenoid sinus or intracranium, even though LC showed no significant difference. It is hard to explain the reason why invasion of the frontal or sphenoid sinus or intracranium was associated with only OS for a few patients in this study. However, 2 patients whose survival was the longest after recurrence (31M and 22M) had received chemoradiotherapy to the maxillary and ethmoid sinus recurrence and surgery to the ethmoid sinus recurrence, respectively. Those patients had originally no invasion of the frontal or sphenoid sinus or intracranium, accordingly local recurrent tumor was treated by radical treatment. Patients whose tumor does not have superior or posterior extension have several treatment options even though local recurrence is found and OS might be prolonged.

The incidence of late toxicity was not as high as expected. Two cases showed late toxicity symptoms with a severity of more than Grade 3. One case with brain necrosis had a frontal sinus tumor with invasion of the frontal lobe. The irradiation schedule was a total of 45 Gy of X-ray over 25 fractions and 33 GyE of proton beam over 20 fractions during a 45-day period; the tumor was well controlled, and distant metastasis was not subsequently found. Psychiatric symptoms were first observed at approximately 20 months after treatment, and brain necrosis was found in the right frontal lobe at 21 months. This patient died at 22 months after treatment as a result of acute cardiac insufficiency. Another case with blindness had a huge tumor in the left maxillary sinus with orbital invasion, and most of the left orbital apex was occupied by the tumor. Proton beams were delivered for a total of 77.22 GyE over 39 fractions during a 64-day period. This patient had consented to a loss of vision in the left eye. Keratitis was observed at 9 months after treatment, and severe visual loss was observed after 14 months. The tumor was well controlled, and right eyesight was maintained. This patient is still alive at 64 months after treatment as of January 2011.

The patient (Case 4) who received the highest irradiation dose to the ipsilateral optic nerve (D_{95} 80.2 GyE) and brain surface (D_{95} 81.4 GyE) had tumor invasion of the ipsilateral orbita as well as intracranium and had already lost ipsilateral eyesight at the beginning of treatment. The ipsilateral orbital gland and optic gyrus in the frontal lobe were included in the CTV, and high-dose proton beam irradiation to the critical organ was performed with the patient's consent. A local recurrence was found 4 months after PBT, and chemotherapy was performed. However, no treatment effect was observed, and this patient died 12 months after undergoing PBT.

We previously reported data for head-and-neck cancer patients treated between 1983 and 2000 at a physical research institute close to our institution (19). Irradiation was limited to two to three times per week, and only horizontal and vertical beams were available at that time. Therefore, the treatments were performed with a relatively high-dose fraction rate (the dose fraction was 3.3 GyE in the proton beam-only group and 1.8 Gy of X-ray plus 2.75 GyE of proton beam in the combined X-ray and proton group; the total irradiation dose was 81.8 GyE). Twenty-one percent of the patients had severe late toxicity in our previous study (mostly ulcerations of the irradiated skin or mucosa and osteonecrosis). We started treatments in our new hospital-based facility in 2001, at which time irradiation 5 days per week and the use of a rotating gantry became feasible. The dose fraction rate was reduced to 2.2 GyE per day, and many patients were treated using multiple ports including an oblique beam direction. We believe that the lower incidence of ulceration and osteonecrosis was made possible by the reduction of the dose fraction rate and the dispersal of the irradiation dose to the surrounding bone, skin, and mucosa.

Our study has some limitations as a result of its retrospective design. Furthermore, some of the patients entered hospice care after suffering a recurrence and were lost to follow-up at our hospital. Moreover, some patients who received a high irradiation dose to a critical organ might have had a short survival period, dying before late toxicity was revealed. Nevertheless, the present study indicates the safety of PBT with a D_{95} of <50 GyE to the optic chiasm and contralateral optic nerve and a fractionation schedule of 2.2 GyE per day using multiple beam directions to the

Table 4 Dose–volume histogram analysis

Factor	Volume (cm^3)	D_{max} (GyE)	D_{05} (GyE)	D_{95} (GyE)
Ipsilateral optic nerve	0.8	83.0–22.2 (74.4) 77.4*	82.3–22.0 (74.0) 77.3*	80.2–6.3 (64.6) 69.3*
Contralateral optic nerve	0.7	76.3–2.6 (35.9)	75.4–1.7 (31.9)	44.7–0 (7.2)
Optic chiasm	1.6	73.6–0.3 (47.0)	70.9–0 (43.2)	50.9–0 (9.1)
Brain stem	18.2	74.5–0 (52.4)	67.8–0 (20.0)	1.7–0 (0)
Ipsilateral brain surface	6.7	83.8–60.8 (75.9) 78*	82.8–56.4 (74.0) 78*	81.4–0.7 (33.5) 78*

The data represents the volume, D_{max}, D_{05} and D_{95} in the critical organ. The dose data represents maximum-minimum (medium).

* Data pf patients who had late toxicity more than Grade 3.

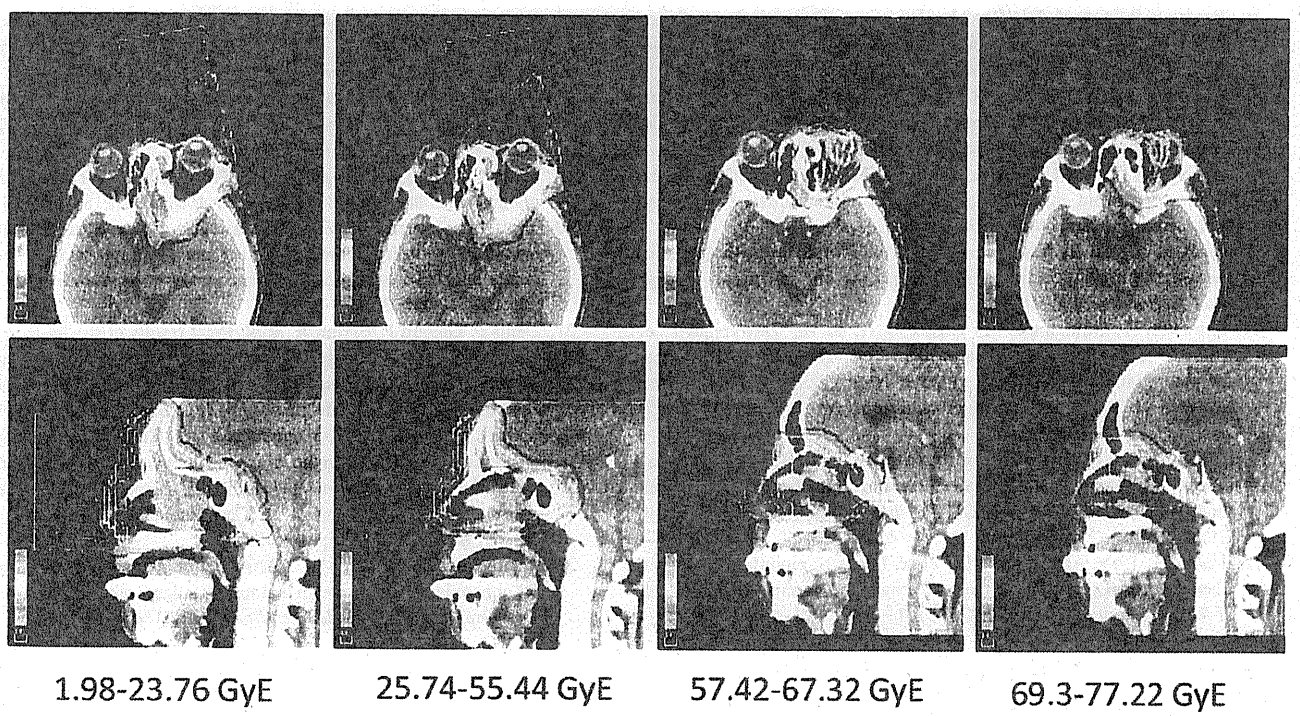

Fig. 4. Dose distribution of a left maxillary sinus carcinoma (T4aN0M0, Stage IVA; upper: axial, middle; lower: sagittal image). Huge tumor occupied the left maxillary sinus, nasal cavity, and ethmoid sinus and invaded into the left orbita. Dose distribution line represents 10%, 20%, 30%, 40%, 50%, 60%, 70%, 80%, 90%, 95%, and 105% from outside to inside. Treatment planning was modified three times during the treatment course, and a total of 77.22 GyE over 39 fractions was irradiated. This image shows the first to last plan from the left. Dose distribution of optic chiasm and brainstem was clearly spared (D_{max} 40.6 GyE, D_{05} 32.2 GyE, D_{95} 0 GyE of optic chiasm; D_{max} 29.3 GyE, D_{05} 3.2 GyE, D_{95} 0 GyE of brainstem).

bone, skin, and mucosa in patients with unresectable carcinoma of the NCPS.

We describe how the outcome of unresectable NCPS carcinoma can be improved. The superiority of concurrent chemotherapy over radiotherapy alone has now been well established (20–22). We did not use chemotherapy in most of the patients in the present series because treatment during this period was performed as part of a clinical trial, and the effects of chemotherapy combined with PBT were not fully recognized. In recent years we have begun concurrent chemotherapy, and the prognosis of patients is expected to improve as a result. All treatment was performed using coplanar proton beams because geometric certainty was not fully verified at that time. However, possible isocentric error and range uncertainty was confirmed about 1 mm in our system (23). We use noncoplanar proton beams to the tumor that is located very close to the critical organs. Technical improvements could accomplish the more conformal and sufficient dose delivery to the tumor and contribute to the outcome. Metastasis to lymph nodes in the neck was found in 4 patients after treatment. Three of these metastases were found 2 months after PBT. We strongly suspect that these metastases were already present at the beginning of treatment. We routinely performed computed tomography and magnetic resonance imaging examinations, and ultrasound and [^{18}F]-fluorodeoxyglucose positron emission tomography were used in some patients. The development of diagnostic techniques using multiple modalities may help to select patients in whom lymph node treatment in the neck is necessary, thereby improving the outcome of patients with carcinoma of the NCPS.

References

1. Silverberg E, Grant RN. Cancer statistics, 1970. *CA Cancer J Clin* 1970;20:11–23.
2. Blanco AI, Chao KS, Ozyigit G, *et al.* Carcinoma of paranasal sinuses: Long-term outcomes with radiotherapy. *Int J Radiat Oncol Biol Phys* 2004;59:51–58.
3. Dulguerov P, Jacobsen MS, Allal AS, *et al.* Nasal and paranasal sinus carcinoma: Are we making progress? A series of 220 patients and a systematic review. *Cancer* 2001;92:3012–3029.
4. Hoppe BS, Stegman LD, Zelefsky MJ, *et al.* Treatment of nasal cavity and paranasal sinus cancer with modern radiotherapy techniques in the postoperative setting—The MSKCC experience. *Int J Radiat Oncol Biol Phys* 2007;67:691–702.
5. Chen AM, Daly ME, Bucci MK, *et al.* Carcinomas of the paranasal sinuses and nasal cavity treated with radiotherapy at a single institution over five decades: Are we making improvement? *Int J Radiat Oncol Biol Phys* 2007;69:141–147.
6. Dirix P, Vanstraelen B, Jorissen M, *et al.* Intensity-modulated radiotherapy for sinonasal cancer: Improved outcome compared to conventional radiotherapy. *Int J Radiat Oncol Biol Phys* 2010;78: 998–1004.
7. Mizoe JE, Tsujii H, Kamada T, *et al.* Dose escalation study of carbon ion radiotherapy for locally advanced head-and-neck cancer. *Int J Radiat Oncol Biol Phys* 2004;60:358–364.
8. Hoppe BS, Nelson CJ, Gomez DR, *et al.* Unresectable carcinoma of the paranasal sinuses: Outcomes and toxicities. *Int J Radiat Oncol Biol Phys* 2008;72:763–769.
9. Suit H, Urie M. Proton beams in radiation therapy. *J Natl Cancer Inst* 1992;84:155–164.

10. Pommier P, Liebsch NJ, Deschler DG, *et al.* Proton beam radiation therapy for skull base adenoid cystic carcinoma. *Arch Otolaryngol Head Neck Surg* 2006;132:1242–1249.
11. Weber DC, Chan AW, Lessell S, *et al.* Visual outcome of accelerated fractionated radiation for advanced sinonasal malignancies employing photons/protons. *Radiother Oncol* 2006;81:243–249.
12. Truong MT, Kamat UR, Liebsch NJ, *et al.* Proton radiation therapy for primary sphenoid sinus malignancies: Treatment outcome and prognostic factors. *Head Neck* 2009;31:1297–1308.
13. Zenda S, Kohno R, Kawashima M, *et al.* Proton beam therapy for unresectable malignancies of the nasal cavity and paranasal sinuses. *Int J Radiat Oncol Biol Phys.* In press.
14. Shirasaka T, Shimamato Y, Ohshimo H, *et al.* Development of a novel form of an oral 5-fluorouracil derivative (S-1) directed to the potentiation of the tumor selective cytotoxicity of 5-fluorouracil by two biochemical modulators. *Anticancer Drugs* 1996;7: 548–557.
15. Cox JD, Stetz J, Pajak TF. Toxicity criteria of the Radiation Therapy Oncology Group (RTOG) and the European Organization for Research and Treatment of Cancer (EORTC). *Int J Radiat Oncol Biol Phys* 1995;31:1341–1346.
16. Daly ME, Chen AM, Bucci MK, *et al.* Intensity-modulated radiation therapy for malignancies of the nasal cavity and paranasal sinuses. *Int J Radiat Oncol Biol Phys* 2007;67:151–157.
17. Dirix P, Nuyts S, Vanstraelen B, *et al.* Post-operative intensity-modulated radiotherapy for malignancies of the nasal cavity and paranasal sinuses. *Radiother Oncol* 2007;85:385–391.
18. Madani I, Bonte K, Vakaet L, *et al.* Intensity-modulated radiotherapy for sinonasal tumors: Ghent University Hospital update. *Int J Radiat Oncol Biol Phys* 2009;73:424–432.
19. Tokuuye K, Akine Y, Kagei K, *et al.* Proton therapy for head and neck malignancies at Tsukuba. *Strahlenther Onkol* 2004;180:96–101.
20. Fortin A, Caouette R, Wang CS, *et al.* A comparison of treatment outcomes by radiochemotherapy and postoperative radiotherapy in locally advanced squamous cell carcinomas of head and neck. *Am J Clin Oncol* 2008;31:379–383.
21. Denis F, Garaud P, Bardet E, *et al.* Final results of the 94-01 French Head and Neck Oncology and Radiotherapy Group randomized trial comparing radiotherapy alone with concomitant radiochemotherapy in advanced-stage oropharynx carcinoma. *J Clin Oncol* 2004;22:69–76.
22. Pignon JP, Bourhis J, Domenge C, *et al.* Chemotherapy added to locoregional treatment for head and neck squamous-cell carcinoma: Three meta-analyses of updated individual data. MACH-NC Collaborative Group. Meta-Analysis of Chemotherapy on Head and Neck Cancer. *Lancet* 2000;355:949–955.
23. Mizumoto M, Nakayama H, Tokita M, *et al.* Technical considerations for noncoplanar proton-beam therapy of patients with tumors proximal to the optic nerve. *Strahlenther Onkol* 2010;186:36–39.

ELSEVIER

Int. J. Radiation Oncology Biol. Phys., Vol. ■, No. ■, pp. 1–8, 2011

0360-3016/$ - see front matter

doi:10.1016/j.ijrobp.2010.10.028

CLINICAL INVESTIGATION

INVESTIGATION OF THE GEOMETRIC ACCURACY OF PROTON BEAM IRRADIATION IN THE LIVER

NOBUYOSHI FUKUMITSU, M.D.,* TAKAYUKI HASHIMOTO, M.D.,* TOSHIYUKI OKUMURA, M.D.,* MASASHI MIZUMOTO, M.D.,* ERIKO TOHNO, M.D.,† KUNIAKI FUKUDA, M.D.,‡ MASATO ABEI, M.D.,‡ TAKEJI SAKAE, PH.D.,* AND HIDEYUKI SAKURAI, M.D.*

*Proton Medical Research Center, †Department of Radiology, and ‡Department of Gastroenterology, Graduate School of Comprehensive Human Sciences, University of Tsukuba, Tsukuba, Japan

Purpose: To investigate the geometric accuracy of proton beam irradiation to the liver by measuring the change in Hounsfield units (HUs) after irradiation.

Methods and Materials: We examined 21 patients with liver tumors who were treated with respiratory-gated proton beam therapy (PBT). The radiation dose was 66 GyE in 12 patients and 72.6 GyE in 9 patients. Image registration and reslicing of the computed tomography (CT) results obtained within 1 month before and 3 months after PBT was performed, referring to the planning CT image. The resliced CT images obtained after PBT were subtracted from the images obtained before PBT. We investigated whether the area of the large HU change was consistent with the high-dose distribution area using the location of the largest change in HU around the tumor (peak) on the subtracted CT image and the 90% dose distribution area of the planning CT image.

Results: The number of patients ($n = 20$) whose left–right peaks were within the 90% dose distribution area was significantly larger than the number of patients whose anterior–posterior peaks and superior–inferior peaks were within the 90% dose distribution area ($n = 14$, $n = 13$, $p = 0.034$, and $p = 0.02$, respectively). Twelve patients exhibited a peak within the 90% dose distribution area in all directions. Nine of the 11 patients with smaller 90% confidence intervals of the percent normalization of the beam cycle (BC; 90% BC) showed a peak within the 90% dose distribution area in six directions, and this percentage was higher than that among the patients with larger 90% BC (3/10, $p = 0.03$).

Conclusion: The geometric accuracy of proton beam irradiation to the liver was higher in the left–right direction than in the other directions. Patients with an irregular respiratory rhythm have a greater risk of a reduced geometric accuracy of PBT in the liver.

Proton beam therapy, Liver tumor, Image analysis software, Respiratory-gated therapy.

INTRODUCTION

To increase the precision of radiotherapy, reducing geometric uncertainties induced by interfraction setup variations and intrafraction breathing movements that lead to differences between the planned dose distribution and the actually delivered radiation dose are essential. Many methods have been investigated and clinically used to improve the geometric accuracy of irradiation. Methods of managing the interfraction setup variation include the use of daily portal images (1), fiducial markers (2), computed tomography (CT) simulation (3), and video cameras (4). Methods of managing intrafraction breathing movements include the use of breath control (5), respiratory-gated radiotherapy (6), and a tumor-tracking system (7).

A variety of methods have been reported for monitoring the interfraction setup variation including the isocenter dose reproducibility (8), repeated radiographs (9), and repeated CT examinations (10). A variety of methods have also been reported for monitoring intrafraction breathing movements, such as diaphragm movements during fluoroscopy (11), tumor movement from CT (12), dose–volume histograms (13), and calculation of the geometric error based on respiratory motion data (14). Moreover, not only interfraction setup variations and intrafraction breathing movements, but also the changes in Hounsfield units (HU) during

Reprint requests to: Nobuyoshi Fukumitsu, M.D., Proton Medical Research Center, University of Tsukuba, 1-1-1, Tennoudai, Tsukuba, 305-8575, Japan. Tel: 81-29-853-7100; Fax: 81-29-853-7102; E-mail: fukumitsun@yahoo.co.jp

Conflict of interest: none.

Acknowledgments—This work was supported by Grant-in aid for Scientific Research (B) No.21390338 from the Ministry of Education, Culture, Science and Technology. We appreciate Hideaki Hayashi in AJS Inc., Japan, Andrew K. Lee, MD in the Department of Radiation Oncology, and Wayne D Newhauser, PhD in the Department of Radiation Physics, The University of Texas MD Anderson Cancer Center, USA for valuable advice.

Received June 25, 2010, and in revised form Sept 21, 2010. Accepted for publication Oct 2, 2010.

breathing (15), mechanical response delays (14), and tumor volume changes during the treatment course may change the dose distributions. Hence, the accuracy of the dose delivery is too complex to be confirmed or predicted based solely on an evaluation of the setup or breathing movements only. To our knowledge, radiographic investigation of the geometric accuracy for quantitatively assessing the radiation dose delivery to the tumor has not been previously reported.

Hypoattenuation of the irradiated areas on CT images occur after hepatic irradiation (16). In proton beam therapy (PBT), the proton beam allows a rapidly increasing dose at the end of the beam range (17). Excellent dose localization of the proton beam causes a clearly distinguishable hypoattenuation area in and surrounding the tumor after irradiation (18). Hence, the HU of the liver tissue surrounding the tumor should be markedly reduced after PBT. In contrast, the HU inside the liver tumor should not be as markedly reduced, as it was relatively low before treatment. Consequently, if a CT image obtained after PBT is subtracted from that obtained before PBT, the profile curve of the reduction in HU should appear as two high peaks with a low-value zone in between, representing the periphery and the inside of the tumor during proton beam exposure, respectively. We hypothesized that the localization of the high-value zones and the low-value zone on the profile curve of the reduction in HU should represent the boundary of the tumor and the surrounding normal liver tissue during radiation exposure, enabling the geometric accuracy of the actual irradiation to be verified.

The aim of this study was to investigate the geometric accuracy of proton irradiation to the liver by examining the locations of the areas with large HU changes on a subtraction CT image.

METHODS AND MATERIALS

Patients and procedures

We analyzed data for 21 liver tumor patients (mean age, 65.0 years; range, 48–78 years; 15 men and 6 women) who underwent PBT between July of 2005 and December of 2007 at the University of Tsukuba (Tsukuba, Japan). The selection criteria included patients with a constant irradiation field and any field size or beam angle that was not changed during the course of treatment. Patients with any other prior or concomitant irradiation were excluded. A CT examination was performed within 1 month before and 3 months after PBT using the same CT scanner (IDT16; Philips Electronics Japan Medical Systems, Bothell, WA). The diagnosis was hepatocellular carcinoma (HCC) in 20 patients and liver metastasis in 1 patient.

Before the start of treatment, metallic fiducial markers were implanted percutaneously into the hepatic parenchyma adjacent to the tumor in 18 patients. A drainage tube, gallstone, and the diaphragm were used as substitute markers in 3 patients in whom metallic fiducial markers were not implanted. Custom-made body casts (ESFORM; Engineering Systems, Matsumoto, Japan) were created to ensure adequate immobilization of each patient during radiotherapy. A treatment planning CT examination (CT [plan]) was performed 1 week before PBT using a CT scanner (W3000AD; Hitachi Medical Corporation, Tokyo, Japan). An abdominal CT scan was obtained using a respiratory-gated acquisition protocol. The respiratory waveform was obtained from a laser displacement sensor that could be focused on an area around the patient's navel. A gate signal was given to enable exposure once the respiratory waveform dropped below a certain threshold. The start of exposure was triggered by the gate signal (Fig. 1). To achieve this, the CT table was moved to the next slice position after scanning. All of the slices (5-mm thick) were scanned downward from the top of the diaphragm. The pitch was 0.5.

A clinical target volume (CTV) was contoured as the gross tumor volume plus a 5- to 10-mm margin on serial CT images. An additional 4- to 6-mm margin in the inferior direction was added to the CTV as an internal margin for respiratory movement. The planning target volume was defined as an internal target volume plus a 7- to 13-mm margin (7 mm, 2 patients; 8 mm, 11 patients; 10 mm, 7 patients; 13 mm, 1 patient) in all directions.

Proton beams of 155 to 250 MeV were generated using a synchrotron accelerator at the Proton Medical Research Center, University of Tsukuba. The beams were delivered under respiratory gating through one to three ports using a rotational gantry. During each treatment session, the positional relationship between the isocenter and the fiducial markers was examined using the orthogonal fluoroscopy unit attached to the treatment unit. The dose distribution was calculated using a pencil beam algorithm. The beam delivery devices, including a ridge filter and a fine degrader, were selected automatically by the treatment planning system. A collimator to shape the lateral edge of the field was produced using a brass array.

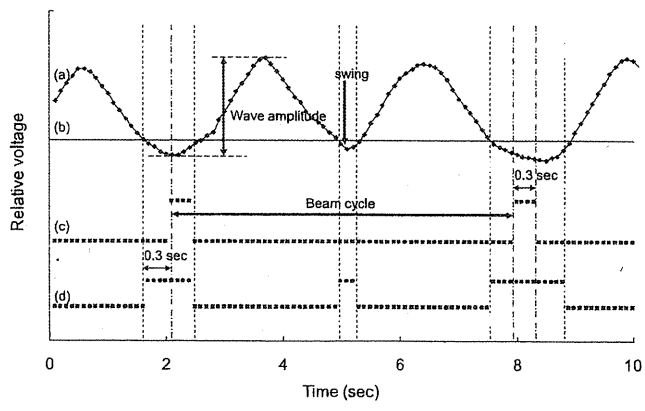

Fig. 1. Time chart of respiratory gated proton beam therapy (PBT). (A) Respiratory waveform. (B) Threshold level of gating. (C) Timing of proton beam exposure. (D) Gate signal. Proton beam is delivered 0.3 s after waveform drops below threshold for 0.3 s.

A range-compensating bolus was fabricated with a tissue-equivalent material. The beam delivery system created a 100% dose level homogeneously using the spread-out Bragg peak of the proton beams. The irradiation dose was 66 Gray equivalents (GyE) over 10 fractions in 12 patients whose tumors were located more than 2 cm from the porta hepatis and digestive tract, and 72.6 GyE over 22 fractions in 9 patients whose tumors were located within 2 cm from the porta hepatic (19, 20).

An abdominal CT examination for diagnosis was performed using a 16-multidetector CT scanner (IDT16) within 1 month before and 3 months after PBT (CT [pre], CT [post], respectively). The abdominal CT scans were obtained using a breath-hold acquisition protocol. A slice thickness of 2 mm with a pitch of 0.9 was continuously scanned, and the data were reconstructed for viewing using a 5-mm slice thickness with a slice interval of 5 mm. We used CT images without contrast enhancement in this study.

The data analysis was performed using the Dr. View/LINUX image analysis software system (AJS, Tokyo, Japan). Liver surface segmentation was performed using an algorithm developed by Alpert *et al.* (21). In short, the threshold values of the lower and upper limits were set at 10 and 80 HU to separate the surrounding organs from the liver. After the thresholding operation, all the pixels inside the largest cluster, *i.e.*, the liver, were filled. Next, the remaining extraliver clusters with a width of connection of less than three pixels were removed from the largest cluster. Finally, the areas that were obviously different from the liver, *i.e.*, the lateral abdominal wall or heart, were erased manually, and the bitmap image of the liver was completed. The image of the liver was constructed by subtracting the outside of the bitmap of the liver from the original CT image. These procedures were all performed using the CT (plan), (pre), and (post) images (Liver [plan], [pre], and [post], respectively].

After liver surface segmentation, we performed image registration of the Liver (pre) and Liver (post) images using the Liver (plan) as a reference. For the image registration, we used a three-dimensional rigid registration algorithm developed by Maes et al. (22). The corresponding voxel intensities were maximized once both images were geometrically aligned, and the Liver (pre) and Liver (post) images were three-dimensionally registered at the same position relative to the Liver (plan) image. Next, the Liver (pre) and Liver (post) images were resliced at the same slice level as the Liver (plan) images. Finally, the resliced Liver (post) image was subtracted from the resliced Liver (pre) image, and the subtraction CT image that showed the decreased HU for each pixel of the liver was completed (Fig. 2).

In the subtraction CT image, belt-like areas of large HU changes were observed around the tumor, as shown in Fig. 3. We defined

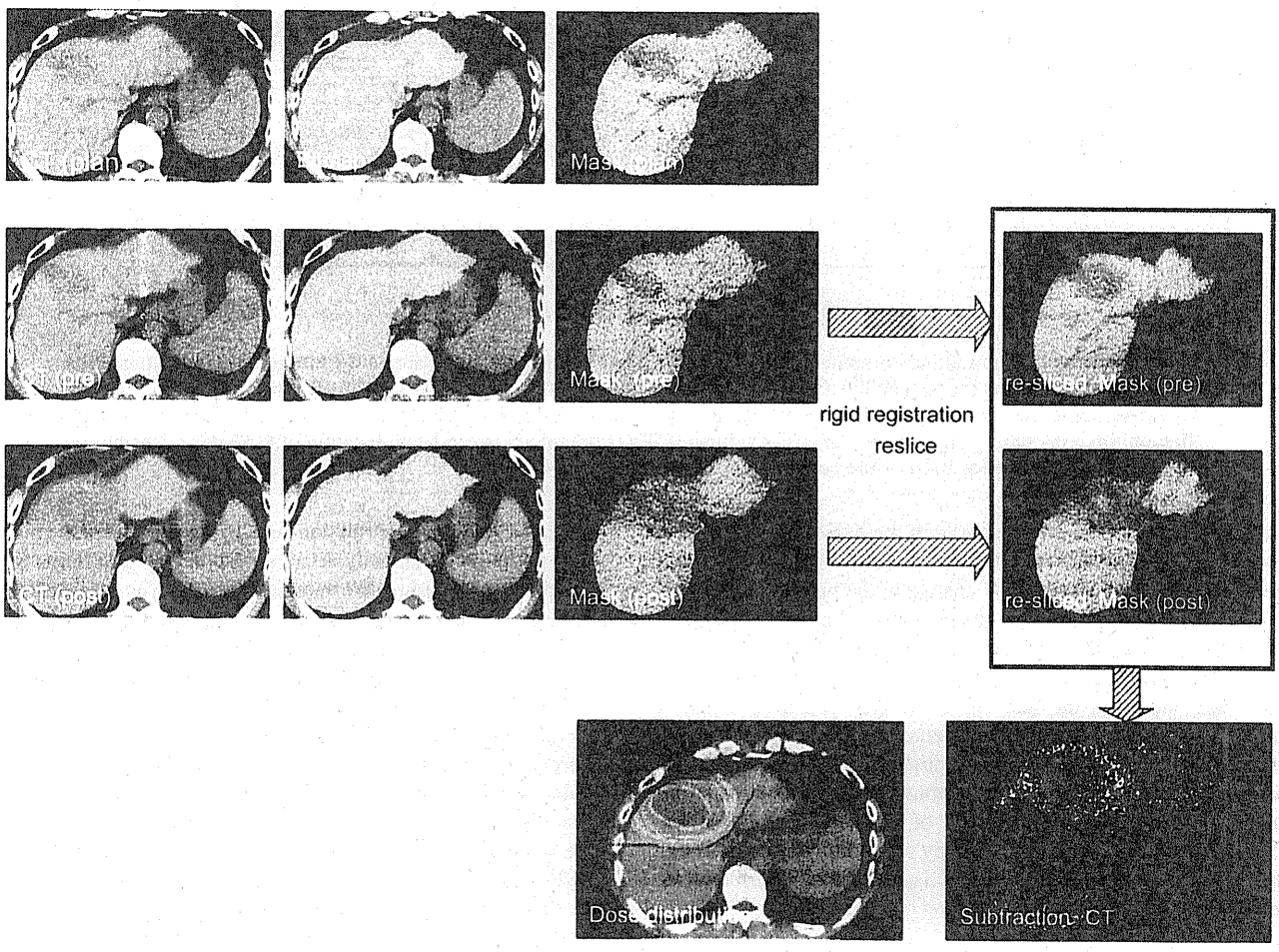

Fig. 2. Process of subtraction computed tomography (CT). The Liver image is constructed by subtracting the outside of the bitmap of the liver from the original CT image. Three dimensional rigid registration of the Liver (pre) and Liver (post) as a reference of the Liver (plan) are done. Liver (pre) and Liver (post) are re-sliced in the same slice level of Liver (plan). The resliced Liver (post) is subtracted from the re-sliced Liver (pre). Subtraction CT that showed the decreased Hounsfield units (HU) in the liver was completed.

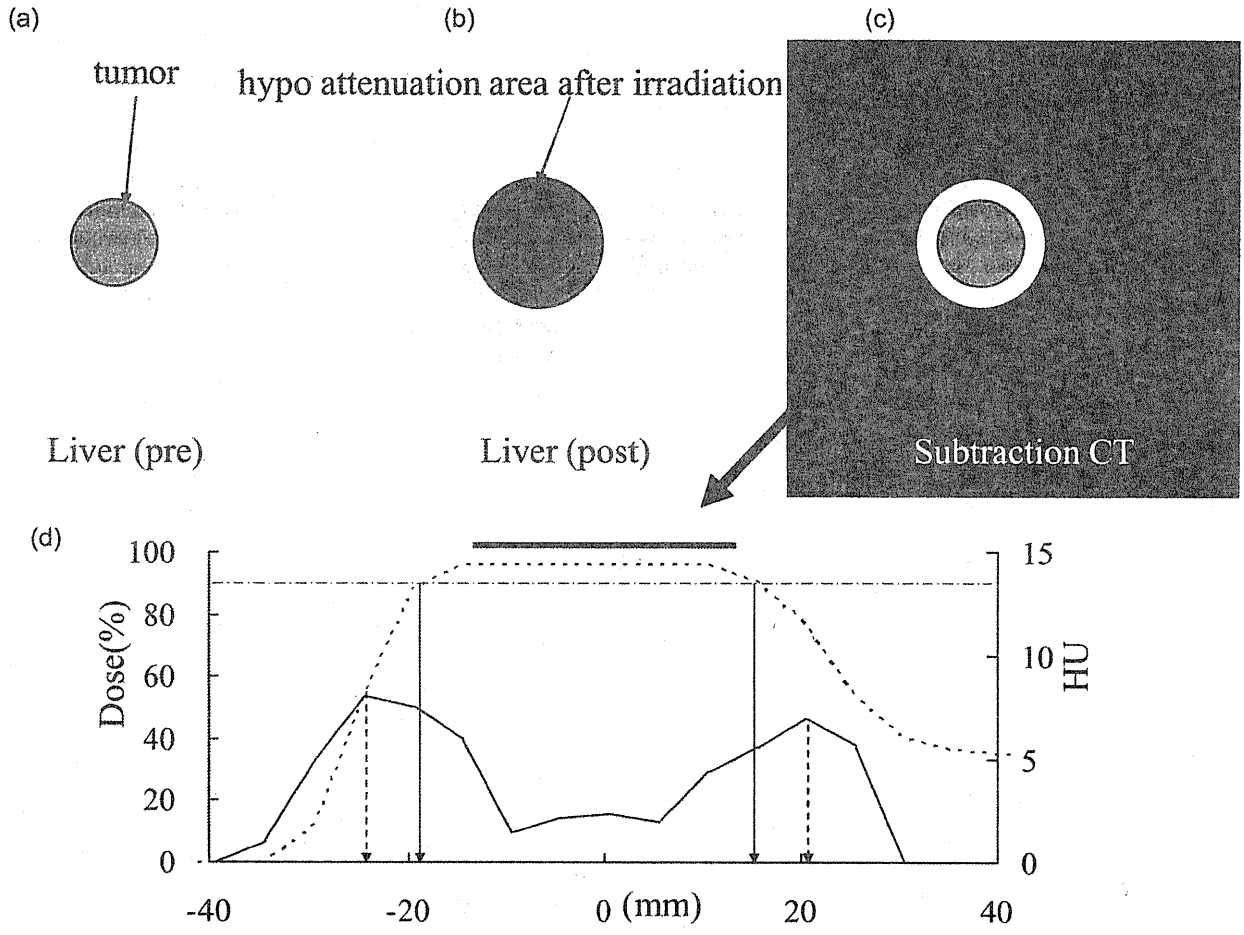

Fig. 3. Schema of subtraction computed tomography (CT). (A) Hypoattenuation area in the tumor. (B) Hypoattenuation area after proton beam therapy (PBT). (C) Decreased Hounsfield units (HU) area surrounding the tumor. (D) Profile curve of the decreased HU and dose distribution. Dotted line indicates dose distribution; solid line indicates HU change. Straight line on top represents range of clinical target volume (CTV). Dotted arrows indicate location of 90% dose distribution; solid arrows indicate location of the peak.

a reference point in the profile curve of the decreased HU and the dose distribution as described below. We identified the location of the peak with the largest HU change in the profile curve of the decreased HU on the left, right, anterior, posterior, superior, and inferior directions from the isocenter. In the profile curve of the dose distribution, we also identified the location of the 90% isocenter dose distribution on the left, right, anterior, posterior, superior, and inferior directions from the isocenter (Fig. 3). We investigated how accurately the actual high-radiation dose area was geometrically included in the high–dose distribution planned area, the influence on the geometric accuracy of the irradiation, and the relationship of the geometric accuracy to the clinical prognosis using the location of the peak and 90% isocenter dose distribution as reference points.

Data analysis

First, we examined the ratio of the peaks inside the 90% dose distribution area in the left–right (LR), anterior–posterior (AP), and superior–inferior (SI) directions. The Kruskal–Wallis rank test and the Wilcoxon signed-rank test were used to compare the significance of the ratios of peaks inside the 90% dose distribution area in the three directions.

Next, we investigated the influence of the respiratory rhythm, distance from the marker, and tumor location on the ratio of peaks inside the 90% dose distribution area. In the analysis of the respiratory rhythm, we randomly selected respiratory waveforms for 25 proton beam exposures. We measured the beam cycle as the interval of one beam to the next beam and the wave amplitude as the difference between the maximum and minimum points in the waveform of each beam interval (Fig. 1). We calculated the percent normalization of the beam cycle and the wave amplitude in each beam interval, then calculated the 90% confidence intervals of the percent normalization of the beam cycle (BC; 90% BC) and wave amplitude (WA; 90% WA) for scale of respiratory rhythm irregularity. The distance from the marker to the isocenter was obtained from the orthogonal portal radiographs. The tumor location was classified as the anterior, posterior, superior, or inferior portion based on the bifurcation of the portal vein. The Fisher exact probability test was used to compare the significance of the ratios of the peak inside the 90% dose distribution area in the classification of the 90% BC, 90% WA, distance from the marker, and tumor location. We decided on cutoff values that enabled well-balanced numbers of patients in the classifications for 90% BC, 90% WA, and distance from the marker.

Finally, we investigated the influence of clinical follow-up data on the ratio of peaks located inside the 90% dose distribution area. The local control rate was calculated using the Kaplan–Meier method, and a log-rank test was performed to compare cases in

which all six peaks were located inside the 90% dose distribution area and cases in which at least one peak was located outside the 90% dose distribution area. Liver damage was classified as hypofunction and no hypofunction according to Child–Pugh classification before and 6 months to 1 year after PBT. The Fisher exact probability test was used to compare the significance of the ratios of peaks located inside the 90% dose distribution area with regard to the classification of liver damage. A value of $p < 0.05$ was considered to indicate a significant difference.

RESULTS

The number of peaks in the profile curve of the decreased HU inside the 90% dose distribution area was 20/21 in the left, 21/21 in the right, 17/21 in the anterior, 17/21 in the posterior, 18/21 in the superior, and 14/21 in the inferior directions. The ratios of both peaks inside the 90% dose distribution area were 20/21 (95.2%) in the LR, 14/21 (66.6%) in the AP, and 13/21 (61.9%) in the SI directions. The ratio was the highest in the LR direction and the lowest in the SI direction ($p = 0.034$ in the LR and AP directions, and 0.02 in the LR and SI directions, respectively). Twelve patients had all six peaks within the 90% dose distribution area (Group A), and 9 patients had at least one peak outside the 90% dose distribution area (Group B). In the peak outside the 90% dose distribution area, the mean distance from the 90% dose distribution area to the peak was 4.0 mm in the LR, 3.4 mm in the AP, and 6.0 mm in the SI directions.

The mean value of the 90% BC was 26.2% (range, 6.5–68.4%) for all of the patients. Among the 11 patients with a 90% BC ≤ 25%, 9 patients were classified in Group A and 2 patients were classified in Group B, whereas among the 10 patients with a 90% BC > 25%, 3 patients were classified in Group A and 7 patients were classified in Group B ($p = 0.03$; Table 1).

Table 1. Patient characteristics

Characteristic	Group A	Group B	*p* Value
90% BC			
≤25%	9	2	0.03
>25%	3	7	
90% WA			
≤5%	7	6	> 0.99
>5%	5	3	
Distance from marker			
≤3 cm	7	6	> 0.99
>3 cm	5	3	
Tumor location (AP)			
Anterior	6	3	0.66
Posterior	6	6	
Tumor location (SI)			
Superior	9	7	> 0.99
Inferior	3	2	
No. of patients	12	9	

Abbreviations: AP = anterior–posterior; BC = beam cycle; SI = superior–inferior; WA = wave amplitude.

Group A refers to patients with all six peaks inside the 90% dose distribution area; Group B refers to patients with at least one peak outside the 90% dose distribution area.

The mean value of the 90% WA was 4.4% (range, 1.4–9.6%). Among the 13 patients with a 90% WA ≤ 5%, 7 patients were classified in Group A and 6 patients were classified in Group B, whereas in the 8 patients with a 90% WA > 5%, 5 patients were classified in Group A and 3 patients were classified in Group B ($p > 0.99$, Table 1).

The mean distance from the marker was 2.8 cm (range, 0.7–7.6 cm). Among the 13 patients with a distance from the marker ≤ 3 cm, 7 patients were classified in Group A and 6 patients were classified in Group B, whereas in the 8 patients with a distance from the marker >3 cm, 5 patients were classified in Group A and 3 patients were classified in Group B ($p > 0.99$, Table 1).

The tumor was located in the anterior portion of the liver in 9 patients, the posterior portion in 12 patients, the superior portion in 16 patients, and the inferior portion in 5 patients. No significant difference of the tumor location was found between the two groups (Table 1).

In Group A, local recurrence was found in 1 patient at 24 months (observation period: median, 26 months; range, 3–49 months). In Group B, local recurrence was found in 1 patient at 27 months (observation period: median, 14 months; range, 3–27 months). No significant difference in the local control rate was observed between the two groups ($p = 0.247$). In Group A, 11 patients showed no hypofunction and 1 patient showed hypofunction according to the Child–Pugh classification. In Group B, 6 patients showed no hypofunction, and 3 patients showed hypofunction ($p = 0.149$).

Figures 4 and 5 plot the reduction in HU and the dose distribution for the patients in Groups A and B, respectively.

DISCUSSION

This study evaluated whether an adequate irradiation dose was actually delivered to the tumor based on the change in HU in the liver. To the best of our knowledge, this is the first study to investigate the accuracy of the actual dose delivery in an noninvasive manner in the liver.

Despite the use of a respiratory-gated or tumor tracking technique, the displacement of the liver occurs in a direction order of SI > AP > LR (2, 13, 23). The ratio of peaks inside the 90% dose distribution area was highest for the LR direction and lowest for the SI direction in our study, consistent with the published findings regarding liver displacement. Moreover, the interfraction setup error in the SI direction tends to be larger than that in the AP and LR directions (2, 24). Taken together, these results suggest that some uncertainty in the dose delivery may exist in directions influenced by large intrafraction breathing movements and interfraction setup variations.

As shown in the present results, patients with a large 90% BC had an increased risk of geometric error. In our system, the proton beam is delivered for approximately 0.3 s after the respiratory waveform drops below a threshold value. However, the proton beam is not always delivered during a constant respiratory phase because of variations in the

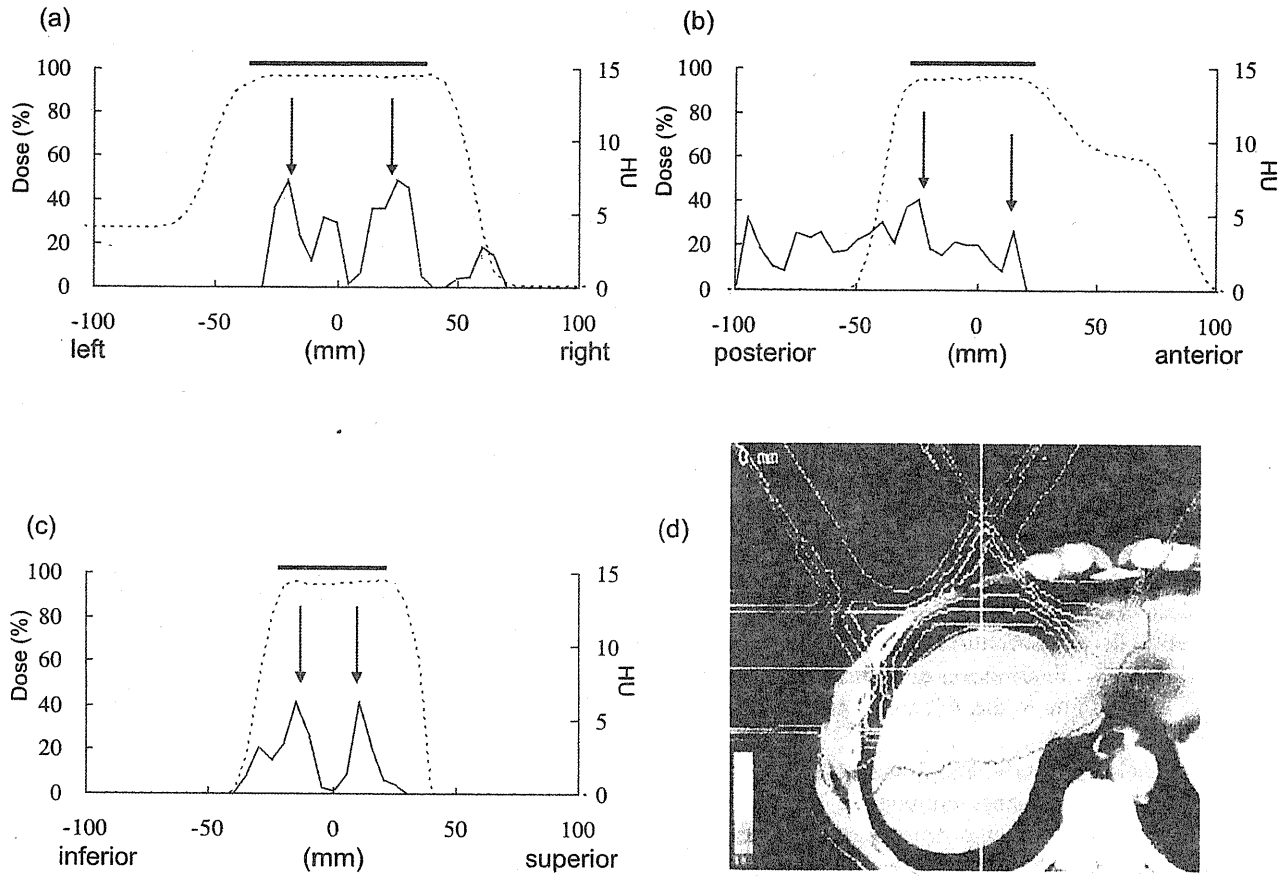

Fig. 4. Profile curve of the decreased Hounsfield units (HU) and dose distribution (Group A). (A) Left–right (LR) direction. (B) Anterior–posterior (AP) direction. (C) Superior–inferior (SI) direction. (D) Dose distribution (axial image). Location of peak is inside 90% dose distribution area in every direction. Value of 90% BC is 6.5%.

respiratory rhythm. Moreover, some patients do not have an adequate respiratory rhythm for respiratory-gated irradiation because of the "swing" phenomenon, in which the proton beam is not delivered despite the respiratory waveform dropping below the threshold because the interval below this threshold was less than 0.3 s. Even if the threshold is set at an adequate level and regular proton beam exposure is expected at the start of the treatment, as the swing time increases, the beam cycle should be varied. In actuality, in this study, the mean number of swing times was 25.3 (range, 5–67) in the 10 patients with a small 90% BC, and 8.3 (range, 0–17) in the 11 patients with a large 90% BC. The swing phenomenon is not directly concerned with actual dose delivery. However, because the swing time is closely related to beam cycle irregularity and can be obtained without requiring complicated calculations during proton beam irradiation, patients with an adequate respiratory rhythm can be identified, or an alternative method, such as feedback-guided breath holding, can be adopted for those patients with extremely irregular respiratory rhythms. The distance from the laser displacement sensor to a point on the body surface changes greatly because the laser beam direction does not always compensate for the body surface movement. The reason why a significant relation was not observed for the 90% WA may be because the wave amplitude does not represent the movement of the organ itself but, rather, the body surface.

In our study, the distance from the marker did not affect the geometric error. The main reason for this is that the location of the marker was close to the tumor in all the patients. Moreover, we double-checked the daily orthogonal portal image using not only the markers but also the spine and/or diaphragm for patient positioning. We believe the setup error was minimal using this system. The liver has less respiratory-induced flexibility than the lung, and lung tumors move differently depending on their location (25). Our results suggest that the tumor location in the liver did not greatly affect the geometric error.

As shown in the results from this study, no significant difference in the local control rate or liver damage was found between patients in Groups A and B. The reasons for these findings are difficult to explain. However, in our previous study, the local control rate was 94.5% at 3 years in a 66 GyE study (19), and 86.0% at 3 years in a 72.6 GyE study (20). Almost all the liver tumors are well controlled locally after PBT. Although liver hypofunction tended to occur frequently in Group B, no significant difference was found. Liver function was well maintained after PBT of the liver tumors, and PBT was fully tolerated by the liver in our previous studies (19, 20). The high local control rate and rarity of

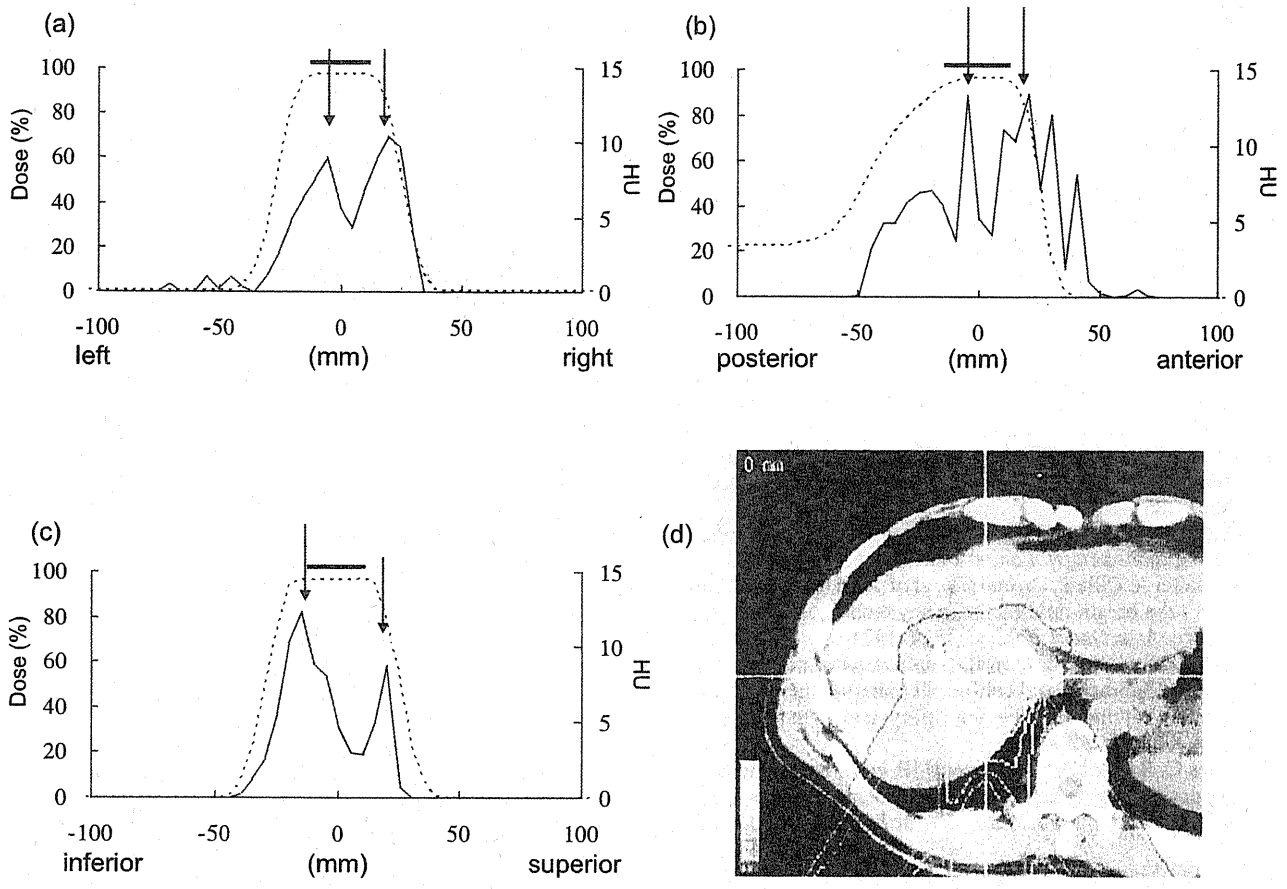

Fig. 5. Profile curve of the decreased Hounsfield units (HU) and dose distribution (Group B). Location of peak is outside of 90% dose distribution area in anterior and superior direction. Value of 90% BC is 39.2%.

liver hypofunction may make it difficult to draw definitive conclusions.

Several problems remain to be solved. First, the image segmentation process involved some manual operations to erase areas that were obviously different from the liver, *i.e.,* the lateral abdominal wall or heart, because the liver was extremely close to the organs, both of which have an HU similar to that of the liver. None of the other processes involved any manual operations, and we considered the quality and reproducibility of the resliced liver images to be sufficient for clinical use. On the other hand, a variety of automated liver segmentation techniques have been rapidly improved and clinically used in recent years (26, 27). A fully automated procedure with no manual operation is not only less time consuming but would enable a more objective estimation and should be performed in the near future. Second, we used rigid registration and image registration of the Liver (pre) and Liver (post) images to the Liver (plan) image. However, liver deformation occurs after radiotherapy (28). The error derived from deformation should be as small as possible. We used CT (post) images that were acquired within 3 months after PBT. The figure and shape of the Liver (post) image was quite consistent with the Liver (pre) image in all of the patients. We consider that this technique can be applied using CT images obtained within a few months after PBT, as such images are likely to have both an obvious HU change and a minimal deformation of the liver. However, an investigation using a deformable image registration technique could provide more detailed estimations in the future.

CONCLUSION

In summary, this report investigated the cause of geometric errors in patients with liver tumors treated with PBT using an image analysis method. A large variety of beam intervals cause geometric uncertainties, and patients with extremely irregular respiratory rhythms might require education regarding respiration or should be treated using a larger margin or alternative technique.

REFERENCES

1. Wong J, Yan D, Michalski J, *et al.* The cumulative verification image analysis tool for offline evaluation of portal images. *Int J Radiat Oncol Biol Phys* 1995;33:1301–1310.

2. Kitamura K, Shirato H, Shimizu S, *et al.* Registration accuracy and possible migration of internal fiducial gold marker implanted in prostate and liver treated with real-time tumor-

tracking radiation therapy (RTRT). *Radiother Oncol* 2002;62: 275–281.
3. Wulf J, Hadinger U, Oppitz U, *et al.* Stereotactic radiotherapy of extracranial targets: CT-simulation and accuracy of treatment in the stereotactic body frame. *Radiother Oncol* 2000; 57:225–236.
4. Ploeger LS, Frenay M, Betgen A, *et al.* Application of video imaging for improvement of patient set-up. *Radiother Oncol* 2003;68:277–284.
5. Rosenzweig KE, Hanley J, Mah D, *et al.* The deep inspiration breath-hold technique in the treatment of inoperable non-small-cell lung cancer. *Int J Radiat Oncol Biol Phys* 2000;48:81–87.
6. Ohara K, Okumura T, Akisada M, *et al.* Irradiation synchronized with respiration gate. *Int J Radiat Oncol Biol Phys* 1989;17:853–857.
7. Shirato H, Shimizu S, Shimizu T, *et al.* Real-time tumour-tracking radiotherapy. *Lancet* 1999;353:1331–1332.
8. Piermattei A, Cilla S, Grimaldi L, *et al.* Real time transit dosimetry for the breath-hold radiotherapy technique: An initial experience. *Acta Oncol* 2008;47:1414–1421.
9. Zhao JD, Xu ZY, Zhu J, *et al.* Application of active breathing control in 3-dimensional conformal radiation therapy for hepatocellular carcinoma: The feasibility and benefit. *Radiother Oncol* 2008;87:439–444.
10. Eccles C, Brock KK, Bissonnette JP, *et al.* Reproducibility of liver position using active breathing coordinator for liver cancer radiotherapy. *Int J Radiat Oncol Biol Phys* 2006;64:751–759.
11. Ford EC, Mageras GS, Yorke E, *et al.* Evaluation of respiratory movement during gated radiotherapy using film and electronic portal imaging. *Int J Radiat Oncol Biol Phys* 2002;52:522–531.
12. Patel AA, Wolfgang JA, Niemierko A, *et al.* Implications of respiratory motion as measured by four-dimensional computed tomography for radiation treatment planning of esophageal cancer. *Int J Radiat Oncol Biol Phys* 2009;74:290–296.
13. Langner UW, Keall PJ. Accuracy in the localization of thoracic and abdominal tumors using respiratory displacement, velocity, and phase. *Med Phys* 2009;36:386–393.
14. Vedam S, Docef A, Fix M, *et al.* Dosimetric impact of geometric errors due to respiratory motion prediction on dynamic multileaf collimator-based four-dimensional radiation delivery. *Med Phys* 2005;32:1607–1620.
15. Minohara S, Endo M, Kanai T, *et al.* Estimating uncertainties of the geometric range of particle radiotherapy during respiration. *Int J Radiat Oncol Biol Phys* 2003;56:121–125.
16. Jeffrey RB Jr., Moss AA, Quivey JM, *et al.* CT of radiation-induced hepatic injury. *AJR Am J Roentgenol* 1980;135:445–448.
17. Suit H, Urie M. Proton beams in radiation therapy. *J Natl Cancer Inst* 1992;84:155–164.
18. Ahmadi T, Itai Y, Onaya H, *et al.* CT evaluation of hepatic injury following proton beam irradiation: Appearance, enhancement, and 3D size reduction pattern. *J Comput Assist Tomogr* 1999;23:655–663.
19. Fukumitsu N, Sugahara S, Nakayama H, *et al.* A Prospective Study Of Hypofractionated Proton Beam Therapy For Patients With Hepatocellular Carcinoma. *Int J Radiat Oncol Biol Phys* 2009.
20. Mizumoto M, Tokuuye K, Sugahara S, *et al.* Proton beam therapy for hepatocellular carcinoma adjacent to the porta hepatis. *Int J Radiat Oncol Biol Phys* 2008;71:462–467.
21. Alpert NM, Berdichevsky D, Levin Z, *et al.* Improved methods for image registration. *Neuroimage* 1996;3:10–18.
22. Maes F, Collignon A, Vandermeulen D, *et al.* Multimodality image registration by maximization of mutual information. *IEEE Trans Med Imaging* 1997;16:187–198.
23. Wagman R, Yorke E, Ford E, *et al.* Respiratory gating for liver tumors: Use in dose escalation. *Int J Radiat Oncol Biol Phys* 2003;55:659–668.
24. Dawson LA, Brock KK, Kazanjian S, *et al.* The reproducibility of organ position using active breathing control (ABC) during liver radiotherapy. *Int J Radiat Oncol Biol Phys* 2001;51:1410–1421.
25. Seppenwoolde Y, Shirato H, Kitamura K, *et al.* Precise and real-time measurement of 3D tumor motion in lung due to breathing and heartbeat, measured during radiotherapy. *Int J Radiat Oncol Biol Phys* 2002;53:822–834.
26. Foruzan AH, Zoroofi RA, Hori M, *et al.* A knowledge-based technique for liver segmentation in CT data. *Comput Med Imaging Graph* 2009;33:567–587.
27. Rusko L, Bekes G, Fidrich M. Automatic segmentation of the liver from multi- and single-phase contrast-enhanced CT images. *Med Image Anal* 2009;13:871–882.
28. Brock KK, Sharpe MB, Dawson LA, *et al.* Accuracy of finite element model-based multi-organ deformable image registration. *Med Phys* 2005;32:1647–1659.

Radiotherapy and Oncology 99 (2011) 124–130

Contents lists available at ScienceDirect

Radiotherapy and Oncology

journal homepage: www.thegreenjournal.com

Proton therapy

Displacement of hepatic tumor at time to exposure in end-expiratory-triggered-pulse proton therapy

Yoshiko Oshiro [a,*], Toshiyuki Okumura [a], Masaya Ishida [a], Shinji Sugahara [b], Masashi Mizumoto [a], Takayuki Hashimoto [a], Kiyoshi Yasuoka [a], Koji Tsuboi [a], Takeji Sakae [a], Hideyuki Sakurai [a]

[a] Department of Radiation Oncology and Proton Medical Research Center, Tsukuba University; [b] Department of Radiation Oncology, Tokyo Medical University, Ibaraki, Japan

ARTICLE INFO

Article history:
Received 25 August 2010
Received in revised form 18 April 2011
Accepted 3 May 2011
Available online 26 May 2011

Keywords:
Proton therapy
PTV margin
Respiratory gated radiotherapy
Tumor tracking system
Hepatocelular carcinoma

ABSTRACT

Purpose: This study is to evaluate reproducibility of hepatic tumors in end-expiration and end-inspiration on free-breathing, also measure shift of hepatic tumor location in pulsed proton beams exposure in end-expiration in order to estimate feasible planning target volume (PTV) margin.

Materials and methods: Pairs (1232) of anterior and lateral radiographs from 30 patients (628 end-expiration and 604 end-inspiration phases) were analyzed using fiducial markers adjacent to the tumors. By using the co-ordinates of the marker centroid of mass related to the isocenter, intrafractional variation was compared in end-expiration and end-inspiration, and a feasible PTV margin was generated using the measured motion.

Results: The average internal motion in end-expiration was 1.1 mm, which was significantly smaller than that in end-inspiration. The mean deviation from the plan was −0.1, 0.3, and 0.1 mm in the left–right (LR), cranio–cepharal (CC), and anterior–posterior (AP) directions, respectively. The estimated PTV margins were 3.2, 3.5, and 4.6 mm, in the LR, CC, and AP directions, respectively.

Conclusions: It was indicated that localization of the targets was more reproducibility in end-expiration than that in end-inspiration. Also, feasible and practical margin values were obtained. These should contribute accuracy of respiration synchronized proton radiotherapy for liver tumors.

The role of radiotherapy for liver tumor has increased with recent improvements in the precise radiotherapy, i.e., stereotactic radiotherapy and proton therapy. At Proton Medical Research Center (PMRC) of the University of Tsukuba, proton therapy for liver tumor has been conducted since 1983, and has resulted in a 5-year local control rate >80% [1–5]. The treatment for hepatic tumors in our institute has been conducted with respiratory-gated proton therapy on free-breathing using a synchrotron system. Treatment beams are delivered intermittently during the end-expiratory phase of respiration signal based upon motion measurements at the body surface.

Tumor movement of the liver is of great interest in radiotherapy [6–8]. Various geometrical uncertainties, such as a consequence of breathing, the patients' position, and liver deformation, must be taken into consideration. Moreover, these uncertainties should be investigated in the two stages of parts of continuous beam radiotherapy: continuous tumor movement during respiration, and tumor movement during irradiation based upon a gated radiotherapy system. In addition, tumor position at time to trigger and exposure should also be taken into consideration during respiratory-gated pulse beam treatment. There have been a number of studies reporting of liver tumor movement [9–18]. However, the target position and stability at the fixed respiratory phase has not been established.

Herein, we mathematically analyzed reproducibility of hepatic tumors in end-expiration and end-inspiration on free-breathing, also measure shift of hepatic tumor location in pulsed proton beams exposure in end-expiration in order to estimate feasible planning target volume (PTV) margin.

Materials and methods

Patients and tumor characteristics

Thirty patients (age: 47–85 years, median: 68 years; 27 males and 3 females) were selected randomly from a group of patients with hepatic tumors for this analysis. Their body mass index (BMI) was ranged 19.2–30.0 (median: 22.8). The tumors were located in the right and left lobes in 19 and 11 patients, respectively. Thirteen patients had single and 17 patients had double fiducial markers (size; 2 × 0.5 mm) implanted percutaneously under ultrasonographic guidance adjacent to the tumor before treatment, which enabled on-line evaluation of organ motion [19–21]. The average distance between the isocenters and the markers in the

* Corresponding author. Address: Department of Radiation Oncology, Tsukuba University, Tennodai 1-1-1, Tsukuba, Ibaraki, Japan.
E-mail address: ooyoshiko@pmrc.tsukuba.ac.jp (Y. Oshiro).

0167-8140/$ - see front matter © 2011 Elsevier Ireland Ltd. All rights reserved.
doi:10.1016/j.radonc.2011.05.009

30 patients was 4.2 mm (range: 11.8–96.8 mm) from the planned coordinates.

Procedure of proton beam therapy and verification images

Our facility utilized a synchrotron that produces 250 MeV proton beams. Proton beams with a pulse-width of approximately 0.3 s are extracted from the synchrotron every 2 s. When we treat a target that could be susceptible to respiration-induced motion, the beams are delivered intermittently, synchronized with the respiratory motion of the patient.

In the case of respiratory gating, a respiratory waveform is obtained using a laser range finder that monitors the movement of the patient's body surface. Once a gating signal is developed at a certain point on the respiratory waveform, the accelerator is triggered within 0.1 s and delivers proton beams. In the treatment of hepatic tumors, the gating signal is generally applied to the accelerator to deliver the beams when the respiratory waveform

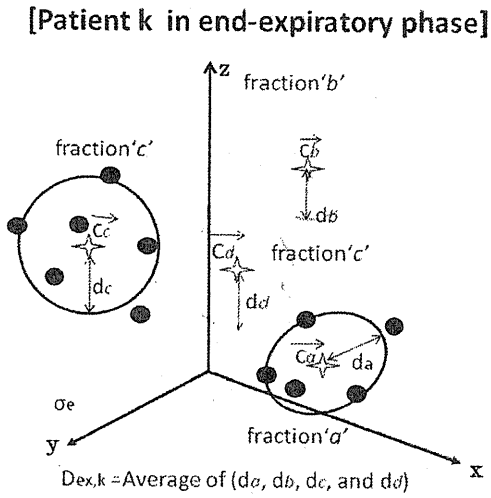

Fig. 1. Intra fraction motion of the marker in patient *k* in four fractions, black dots indicate present observed positions of the marker and corresponding centroids are indicated centrally by the star. The distance between each marker position and the centroid was obtained in each fraction in one patient, and averaged for all fractions. This was repeated for 30 patients at the end of expiration and end inspiration.

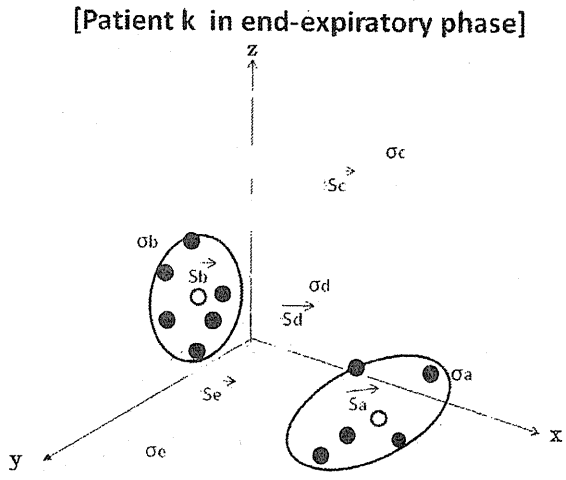

Fig. 2. Random (black dots) and mean (open dot: $\vec{S}_k$) displaced position of the marker with respect to the planned position in the same patient *k*. The SD of the deviation from the treatment plan for each patient is denoted by σ_k.

Table 1
The distance from observed marker positions to the centroids of these markers for each patient (mm).

Patient	1	2	3	4	5	6	7	8	9	10	11	12	13	14	15	16	17	18	19	20	21	22	23	24	25	26	27	28	29	30	Average
Expiration																															
Average	2.1	1.5	1.4	1.2	0.4	1.9	0.9	1.6	0.4	0.9	1.1	1.7	0.6	1.4	0.6	1.0	1.2	1.3	1.5	1.3	1.1	1.1	0.5	0.9	0.8	1.0	1.3	0.6	0.7	0.5	1.1
Max	3.9	4.1	3.3	3.6	0.8	4.4	1.9	3.7	0.9	2.6	2.9	4.3	1.5	4.5	5.0	3.0	5.1	1.3	3.8	5.4	3.7	2.3	1.1	2.8	2.2	4.7	2.9	1.8	1.8	1.2	
Inspiration																															
Average	2.0	5.5	3.3	4.2	1.9	1.4	2.4	1.0	2.3	3.0	1.4	5.5	2.1	4.2	1.3	1.6	2.8	1.3	2.7	4.4	2.7	5.4	1.2	6.8	4.9	2.5	1.4	0.7	1.2	1.1	2.7
Max	4.2	9.2	7.9	10.2	6.5	5.4	9.7	3.0	5.1	7.8	3.7	11.1	4.8	21.5	3.3	4.9	9.6	4.3	7.9	17.4	8.0	14.7	3.3	26.5	18.2	8.0	3.2	2.0	2.9	2.7	

drops below a threshold of 25% for expiration (see Supplementary file-1). The X-ray tube for the fluoroscopic and verification imaging is located within the treatment nozzle, which moves out during the proton irradiation. It is triggered as well as the accelerator: therefore, verification images are taken at the same time as the irradiation (see Supplementary file-2).

The clinical target volume (CTV) was contoured using computer tomography (CT) images of the patient obtained in the treatment position synchronized with the end-expiratory phase. For the planning target volume (PTV), as respiratory margins, uniform 8–10 mm margins and an additional 5 mm caudal margin were added to the CTV. The isocenter was automatically defined as the center of the CTV using the planning system.

Anterior and lateral digitally reconstructed radiographs (DRR) were prepared for target localization. These pretreatment DRRs were the first reference images for both bone alignment and target localization.

Our patient positioning protocol was as follows: the patient position was adjusted prior to treatment based on the body marks on their skin under laser position guidance (LB-300, KEYENCE, Osaka, Japan). On-line correction was subsequently made based on bony landmarks using orthogonal fluoroscopy (DAR-3000; Shimadzu, Kyoto, Japan) with a reference to the pretreatment DRRs. Final adjustment was then made focusing on the position of the fiducial markers. The second set of reference radiographs of end-expiratory phase was subsequently obtained using the image processing unit (DAR-3000, Shimazu, Kyoto, Japan) (see Supplementary file-2). These second reference images were used as an alternative to pretreatment DRRs for the subsequent treatment sessions.

In this study, verification images were also taken in the end-inspiration phase, when the respiratory waveform rose above 75% (see Supplementary file-1).

Data analysis

Acquisition of anterior and lateral verification images, synchronized with both the end-expiration and end-inspiration phase, was performed with the image-processing unit 4–6 times during each fraction, and was repeated randomly in 2–6 fractions for each patient.

Of the 30 patients, the marker positions of 628 events in end-expiration and 604 events in end-inspiration were analyzed. When two markers were implanted, the one nearer to the isocenter was selected for the analysis. The verification images were analysed manually using the MEDISP DICOM Viewer (MEDICAL IMAGE & SIGNAL PROCESSING Lab. Dept. of Medical Instruments Technology, Athens, Greece).

The marker coordinates of the left–right (LR) – cephalad-caudal (CC) position were obtained from anterior images with their origin at the isocenter, and the coordinates of the anterior–posterior (AP) – CC were obtained similarly from lateral images. The CC motion of the markers was averaged for each image pair. We identified the LR, CC, and AP directions as x, y, and z, respectively, and defined the left, cephalad, and anterior aspect of the patient as the positive direction. Using the x, y, z vector, the marker position was assessed as described below. All statistical analyses were performed using commercially available statistical software (SPSS Inc., Chicago, IL, USA).

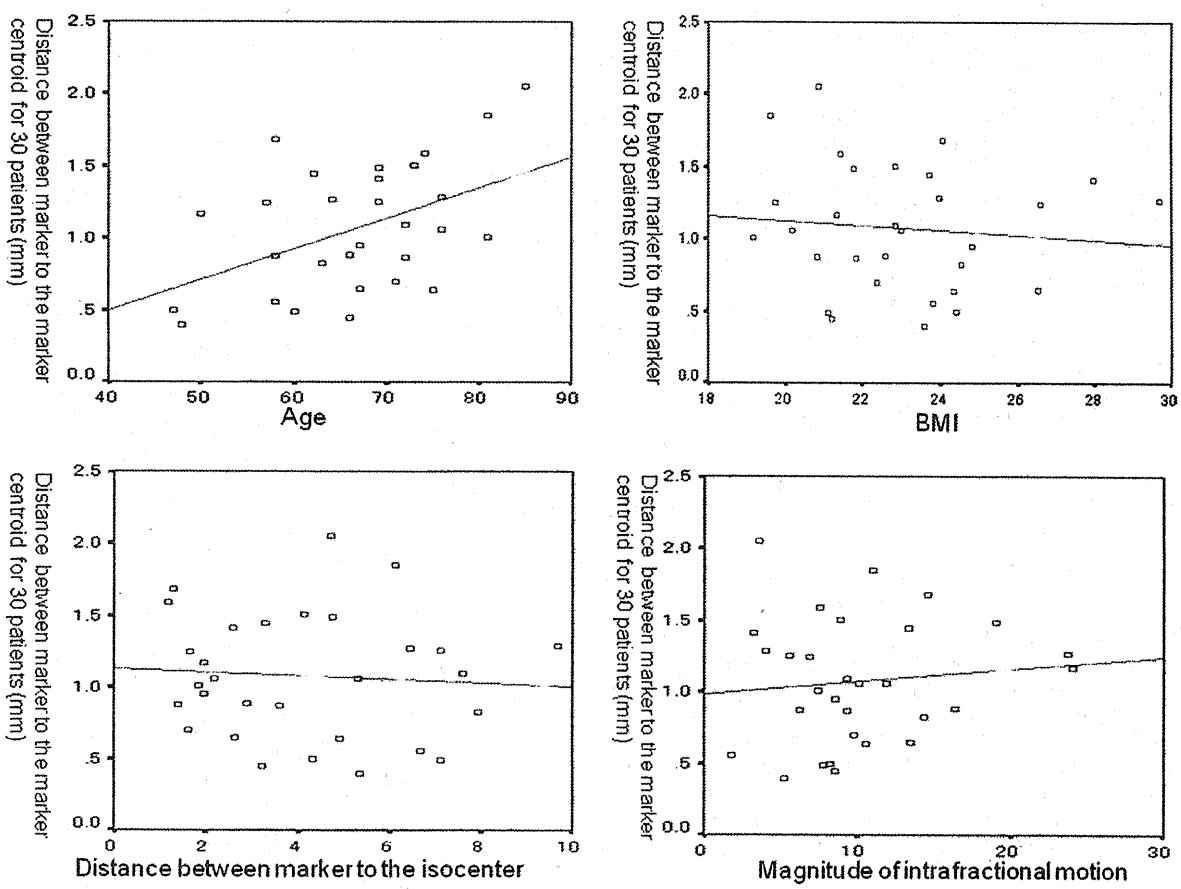

Fig. 3. The correlation between the intrafractional uncertainties and age, BMI, the distance from the isocenter to each marker, and the magnitude of the intrafractional motion.

Intrafractional tumor location at time to exposure

We calculated the intrafractional tumor motion in end-expiration, and also compared to that in end-inspiration. The datasets comprised 628 end-expiration and 604 end-inspiration marker coordinates. In every fraction, the coordinates of the centroid of the observed markers in end-expiration ($\vec{C}_{ex}$) and end-inspiration ($\vec{C}_{in}$) were determined. The vectors from the marker at every fraction to the centroid represent the intrafractional uncertainty. The average distance of the intrafractional uncertainties throughout all fractions for each patient in end-expiration and end-inspiration (D_{ex} and D_{in}) was subsequently calculated; i.e., the D_{ex} and D_{in} indicated the averaged radius of the circle of intrafractional motion for the patient (Fig. 1), and represented the dispersion of the tumor location during the expiratory and inspiratory phases. The D_{ex} and D_{in} for all patients were compared using the two-sample t-test. The magnitude of the intrafractional motion was obtained as the distance between $\vec{C}_{ex}$ and $\vec{C}_{in}$ in each fraction and averaged for each patient. The intrafractional uncertainties was stratified by the extent of patient parameters, (i.e., BMI, age, and tumor location, and averaged magnitude of intrafractional motion) and marker-related parameters (i.e., number of markers and distance from the isocenter) using the Spearman rank method and multivariable analysis.

Deviation of the markers from the planned coordinates at time to exposure in the expiration phase and the calculation of PTV margins

Initially, the deviation between the planned and observed coordinates of the markers in every fraction was calculated, and stratified based on the patient (i.e., age, BMI, and tumor location, and averaged magnitude of intrafractional motion) and the marker-related parameters (i.e., number of markers and distance from the isocenter). The PTV margins were then calculated. Several previous reports have suggested methods for the calculation of the PTV margin [22–27]. Herein, we utilized the definitions of Stroom et al. for the systematic and random errors [23,24,26] of the 628 end-expiration marker coordinates. Systematic and random errors for each patient ($\vec{S}_k$ and σ_k) represented the mean value and standard deviation (SD) of the differences from the treatment plan in the fractionated treatment, respectively, which included set-up and organ motion variation (Fig. 2). The population average and the SD of the systematic error were denoted by μ and Σ, respectively. Furthermore, the random error of the patient group was denoted by σ. Based on these parameters, the PTV margins were calculated as $(2\Sigma + 0.7\sigma)$, where >99% CTV volume was able to cover >95% of the dose [23,24,28,29]. Spearman rank correlation and multivariate analyses were employed for statistical comparisons.

Results

Intrafractional tumor location at time to exposure

The data for each patient are shown in Table 1. The average distance from the observed markers to their centroid in the fraction, which represents the dispersion of the tumor location, in all patients at expiration (D_{ex}) and inspiration (D_{in}) was 1.1 mm (max; 5.4 mm, SD; 0.4 mm) and 2.7 mm (max; 26.5 mm, SD; 1.6 mm). The average magnitude of the intrafractional motion was 10.1 mm (1.8–24.0 mm), respectively. The dispersion of the end-expiration phase was significantly smaller than that of the end-inspiration phase ($p < 0.0001$ by t-test). The intrafractional uncertainties correlated with age (correlation coefficient: $r = 0.41$, $p = 0.024$), but not with BMI ($r = -0.25$, $p = 0.55$), neither the distance between the isocenter ($r = -0.12$, $p = 0.54$), nor the magnitude of the intrafractional motion ($r = 0.12$, $p = 0.573$) (Fig. 3). Furthermore, tumor location, and the number of markers were

Table 2
Deviation from the treatment plan.

Patient	1	2	3	4	5	6	7	8	9	10	11	12	13	14	15	16	17	18	19	20	21	22	23	24	25	26	27	28	29	30	Group mean of S_k (μ)	Group SD of S_k (Σ)	Root mean square of σ_k	Margin (mm) = $2\Sigma + 0.7\sigma$
Deviation from the plan in the fractionated treatment (systematic errors: S_k (mm))																																		
X		−0.8	−0.7	1.1	−0.9	0.7	−1.9	−2.4	−0.3	3.9	−1.5	−1.8	−0.8	−0.6	0.5	0.3	0.0	−0.7	0.7	1.4	0.1	0.8	−0.7	0.3	−1.1	2.5	−0.2	0.4	−0.2	0.2	−0.7	−0.1	1.3		3.2
Y		−0.5	−1.4	0.2	−0.3	0.8	0.8	−1.1	−2.1	1.7	−0.9	0.1	1.7	−0.5	1.0	0.3	−0.5	−0.5	−2.4	1.5	1.2	−0.1	0.7	0.6	−0.6	2.9	0.1	1.0	0.7	1.1	2.6	0.3	1.2		3.5
Z		−3.5	0.4	−0.1	0.6	−1.8	2.1	−1.0	1.5	1.0	−1.8	0.5	−1.6	−0.1	−0.8	2.3	0.1	3.1	−3.3	−1.0	2.7	5.3	−0.7	−0.4	0.8	1.0	2.0	−2.3	−0.8	−0.5	−1.1	0.1	1.9		4.6
SD of the differences in the plan in the fractionated treatment: σ_k (mm)																																		
X		1.1	0.5	1.0	0.9	1.0	1.1	0.8	0.8	0.1	0.6	1.2	0.4	0.7	1.2	0.8	0.1	0.5	0.6	0.7	1.7	0.5	0.7	0.7	0.9	1.1	0.7	1.0	0.5	0.5	0.4			0.8	
Y		2.0	2.3	1.3	1.2	0.8	2.1	1.0	2.7	1.2	1.1	1.5	2.5	0.7	2.3	1.0	0.1	2.2	0.8	1.7	1.7	1.1	1.2	0.8	1.3	1.6	1.4	1.7	0.8	1.0	1.9			1.6	
Z		0.4	0.7	1.1	0.7	0.9	0.9	1.0	0.7	1.1	0.5	0.9	1.8	0.7	0.7	0.7	0.0	1.4	0.5	1.3	2.9	2.6	1.2	0.9	0.8	1.8	0.5	1.2	0.5	0.7	1.0			1.2	

SD: standard deviation.

not significant factors ($p = 0.79$, and 0.18, respectively). Based on multivariate analysis, age was the only significant factor ($p = 0.018$, see Supplementary file-3).

Deviation from planned coordinates at time to exposure in the expiration phase and calculation of the PTV margin

The data from each patient are shown in Table 2. The average deviations from the planned coordinates ($\vec{\mu}$) in the x, y, and z directions for each patient were −0.1 mm (range: −2.4 to 3.9 mm), 0.3 mm (−2.4 to 2.9 mm), and 0.1 mm (−3.6 to 5.3 mm), respectively. Since these deviations are vectors, they are counter-balanced by the positive and negative axes; the absolute values of the deviations were calculated as 0.9 mm, 1.0 mm, and 1.5 mm in the x, y, z directions, respectively. Deviations larger than 5 mm from the DRR were observed in 7 patients (23%) in 30 images (5%). Of these 30 incidents, deviations in excess of 5 mm were observed 0, 9, and 21 times in the x, y, and z directions, respectively. The maximum deviation of all the directions was 9.8 mm in the z-axis. The patients' age correlated with the deviation ($r = 0.399$, $p = 0.023$), but not with BMI, the magnitude of the intrafractional motion, or the distance between the isocenter and the markers ($r = 0.26$, 0.03, and 0.13, respectively: $p = 0.13$, 0.86, and 0.48, respectively); tumor location, and the number of markers were not significant factors ($p = 0.62$, and 0.12, respectively) (Fig. 4). Based on multivariate analysis, none of these factors were significant (see Supplementary file-4).

The SDs of the deviation from the planned coordinates (systematic error: Σ) were 1.3 mm, 1.2 mm, and 1.9 mm, respectively. The group mean of the random error (σ) were 0.8, 1.6, and 1.2 mm, respectively. Based on the ($2\Sigma + 0.7\sigma$), the calculated PTV margins for each component of the x, y, and z axes were calculated as 3.2 mm, 3.5 mm, and 4.6 mm, respectively (Table 2).

Discussion

This is a novel study of patients undergoing gated pulse proton therapy that focused on tumor stability at the time of exposure in 628 and 604 verification images in end-expiration and end-inspiration, respectively.

Nelson et al. investigated lung tumor motion using fiducial markers and an electronic portal imaging device (EPID) [30]. Beddar et al. investigated the correlation between the motions of external and internal fiducial markers implanted in the liver with four-dimensional CT (4DCT) [21]. Using these methods, the actual tumor location at exposure was measured. Instead, we use verification images, because installation of these imaging systems can be difficult during proton therapy because of secondary radiation effects that can influence these devices. The verification images were taken by the X-ray tube triggered as well as the accelerator at the same timing. Therefore, we consider, our results could value the uncertainties of tumor location at exposure.

Consequently, our results indicated that tumor location at a fixed phase in end-expiration was highly reproducible. The results of the higher intrafractional tumor reproducibility in end-expiration compared to that in end-inspiration may suggest that the peak position variation in end-inspiration is greater than that in end-expiration. Age was a significant factor for deviation of the intrafractional tumor location, but not for deviation from the

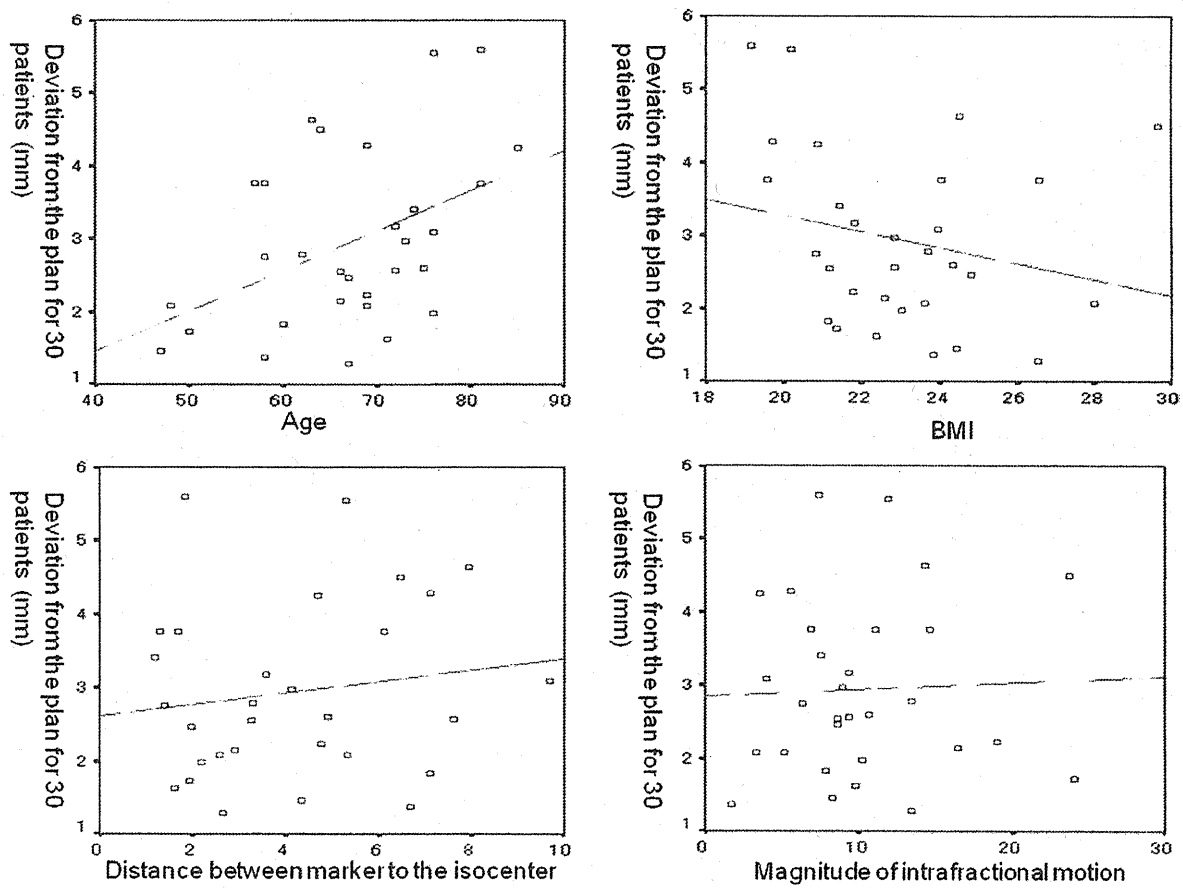

Fig. 4. The correlation between the deviation from the plan and age, BMI, the distance from the isocenter to each marker, and the magnitude of the intrafractional motion.